

# **Computational Scaffold Design for Bone Tissue Engineering: TPMS and Optimized Models**

**Eva Pavão Medeiros**

Thesis to obtain the Master of Science Degree in

## **Biomedical Engineering**

Supervisors: Prof. Paulo Rui Alves Fernandes

Prof. André Paulo Galvão de Castro

### **Examination committee:**

Chairperson: Prof. João Orlando Marques Gameiro Folgado

Supervisor: Prof. Paulo Rui Alves Fernandes

Members of the Committee: Prof. José Arnaldo Pereira Leite Miranda Guedes

**October 2021**



## **Preface**

### Declaration

I declare that this document is an original work of my own authorship and that it fulfills all the requirements of the Code of Conduct and Good Practices of the Universidade de Lisboa.

This work presented in this thesis was performed at Instituto de Engenharia Mecânica of Instituto Superior Técnico (Lisbon, Portugal), during the period February-October 2021, under the supervision of Prof. Paulo Fernandes and Prof. André Castro.



## **Abstract**

Bone is a complex tissue of the human body with a wide variety of functions. Due to its importance, bone tissue engineering has been exploring new methods of facilitating the recovery of damaged bone, among which are scaffolds, a viable method and promising alternative to traditional methods.

Scaffolds are artificially constructed porous support matrices which allow cell seeding, tissue regeneration, and provide mechanical support. These properties are dependent on the microstructure of the scaffold. TPMS geometries and optimized topologies are some of the better choices when it comes to designing these microstructures, but their potentials are not yet fully understood.

To compare these kinds of topologies, a set of TPMS geometries was chosen to compare with a series of optimized geometries created by a topology optimization tool. The optimized geometries were maximized for stiffness and/or permeability. The properties of all these topologies were calculated and compared.

This comparison showed that while TPMS have some favorable properties, optimization tools can offer comparable or even better solutions of scaffold design, on top of being suitable for a wider variety of scenarios.

**Key-words:** Bone Tissue Engineering; Scaffolds; Triply Periodic Minimal Surfaces; Optimization; Permeability; Stiffness



## Resumo

Osso é um tecido do corpo humano complexo e com uma grande variedade de funções. Devido à sua importância, a engenharia de tecidos tem estado a explorar novos métodos de facilitar a regeneração de osso danificado. Um destes métodos são scaffolds, uma alternativa promissora e viável a métodos mais tradicionais.

Scaffolds são matrizes de suporte porosas construídas artificialmente, e que permitem cultura celular, regeneração de tecido, e fornecem suporte mecânico. Estas propriedades estão dependentes na microestrutura das scaffolds. Geometrias TPMS e topologias otimizadas são umas das melhores opções no que toca à criação destas microestruturas. No entanto, as suas capacidades ainda não são totalmente compreendidas.

Para comparar este tipo de topologias, um conjunto de geometrias TPMS foi escolhido para comparar com uma série de geometrias otimizadas criadas por uma ferramenta de optimização de topologia. As geometrias foram maximizadas para permeabilidade e/ou rigidez. As propriedades destas várias topologias foram calculadas e comparadas.

Esta comparação demonstrou que apesar de as TPMS terem propriedades favoráveis, as ferramentas de optimização podem fornecer soluções de design de scaffolds comparáveis ou até melhores, para além de serem adequadas para uma maior variedade de cenários.

**Palavras Chave:** Engenharia de Tecidos Ósseos; Scaffolds; Superfícies Mínimas Triplamente Periódicas; Optimização; Permeabilidade; Rigidez





## **Acknowledgements**

My deepest thanks to all those who helped me throughout this journey.

Firstly, my deepest appreciation to my supervisors Prof. Paulo Fernandes and Prof. André Castro for their guidance and support, for all the knowledge they imparted to me, for the long calls spent in discussion over this work, and for helping me nurture a bigger interest in this field.

No less important was the help of Prof. Rui Ruben and Prof. José Guedes, who were always willing to share their knowledge on their respective fields and offer opinions and suggestions to solve the problems faced along the way.

Additionally, none of this would be possible without my friends. Thank you, Tiago, for initially nudging me into seeking this team and then offering a helping hand; Bárbara and Miguel, for lending a listening ear and motivating me; Wolfe, for all the programming suggestions and the reminders to stay on track; and Forrest, for showing me that it will all be worth it and the reminders to take good care of myself.

And, of course, many thanks to my parents for all their support.



# Index

Preface .....	i
Abstract.....	iii
Resumo .....	v
Acknowledgements .....	vii
Index .....	ix
List of Figures .....	xi
List of Tables .....	xiii
Abbreviations and Symbols .....	xv
1 Introduction .....	2
1.1 Motivation and Objectives .....	4
1.2 Thesis Structure .....	4
2 Literature Review .....	5
2.1 Scaffold Requirements .....	5
2.2 Scaffold Production .....	6
2.2.1 Materials .....	6
2.2.1.1 Metal .....	6
2.2.1.2 Ceramic .....	6
2.2.1.3 Polymers.....	7
2.2.1.4 Composite Materials .....	7
2.2.2 Manufacturing Techniques .....	8
2.2.2.1 Solvent Casting and Particulate Leaching.....	8
2.2.2.2 Gas Foaming .....	9
2.2.2.3 Emulsification Freeze-Drying.....	9
2.2.2.4 Phase Separation .....	9
2.2.2.5 Electrospinning .....	9
2.2.2.6 3D Printing .....	10
2.2.2.7 3D Bioprinting .....	11
2.2.3 Geometry .....	12
2.2.3.1 TPMS.....	12
2.2.3.2 Topology optimization.....	13

3	Methodology .....	15
3.1	Homogenization Theory .....	15
3.1.1	Elasticity Homogenization .....	16
3.1.2	Permeability Homogenization .....	17
3.2	Optimization Tool.....	18
3.2.1	User Variables .....	18
3.2.2	Attribute Calculation .....	20
3.2.2.1	Volume Fraction and Porosity .....	20
3.2.2.2	Relative Permeability .....	20
3.2.2.3	Stiffness FElast.....	20
3.2.3	Problem Formulation .....	20
3.2.4	Implementation .....	22
3.2.5	Problem types.....	24
3.2.5.1	Stiffness optimization problem.....	25
3.2.5.2	Permeability optimization problem.....	25
3.2.5.3	Multi-objective problem.....	26
3.3	CFD Permeability .....	26
3.4	TPMS geometries .....	27
4	Results and Discussion .....	29
4.1	Optimization attribute variability.....	29
4.2	Optimizing TPMS geometries.....	35
4.3	Replication of TPMS properties.....	36
5	Conclusions and Future Work .....	39
5.1	Conclusions .....	39
5.2	Future Work.....	40
	Bibliography .....	41
	Appendix.....	46
	Replication of TPMS properties – full table.....	46

## List of Figures

**Figure 1.1:** Structural details of bone tissue (Tortora & Derrickson, 2016).

**Figure 2.1:** Common scaffold fabrication techniques. A: solvent casting-particle leaching process; B: gas foaming; C: phase separation; D: electrospinning; E: freeze-drying. Adapted from Turnbull et al. (2018).

**Figure 2.2:** Common 3D printing techniques. A: selective laser sintering; B: fused deposition modelling; C: stereolithography. Adapted from Turnbull et al. (2018).

**Figure 2.3:** Common bioprinting techniques. A: inkjet bioprinting; B: laser-assisted; C: microvalve; D: extrusion bioprinting (Turnbull et al., 2018).

**Figure 2.4:** TPMS structures. Right: unit cells of Gyroid, Schwarz D, and Schwarz P TPMS types, adapted from Kladovasilakis et al. (2021). Left: a printed scaffold composed of Schwarz P cells.

**Figure 3.1:** Scheme of the homogenization method. Left: domain of the scaffold  $\Omega^\varepsilon$ ; center: detail of the domain; right: unit cell Y.  $d$  is the characteristic length scale of the microstructure size, represented by  $y$ ;  $D$  is the characteristic length scale of the scaffold, represented by  $Y$ . Adapted from Dias et al. (2014).

**Figure 3.2:** General elasticity problem.

**Figure 3.3:** General flow problem.

**Figure 3.4:** Initial solutions d1 to d8 used in this work.

**Figure 3.5:** Representation of the implementation of the optimization tool.

**Figure 3.6:** Topologies optimized for maximized elasticity, with VF=50% and initial solution d7 (**Figure 3.4**), under different strain fields. Left: uniaxial in x,  $\varepsilon=[1,0,0,0,0,0]$ ; center: uniaxial in y,  $\varepsilon=[0,1,0,0,0,0]$ ; right: biaxial in z/y,  $\varepsilon=[0,1,1,0,0,0]$ .

**Figure 3.7:** Left: cell model resulting from the optimization tool; right: the same cell model in FLUENT® ANSYS®, after addition of the permeability chamber. It is of note that FLUENT® ANSYS® assumes elements not filled with fluid as void, opposite to what is done in the optimization tool.

**Figure 3.8:** TPMS with 70% porosity and cell model size of 20x20x20. Left: SD; middle: SG; right: SP.

**Figure 4.2:** Some of the geometries described in **Table 4.2**. From left to right, top to bottom: d1,  $\alpha=0.2$ , VF=40; d7,  $\alpha=0.2$ , VF=20; d7,  $\alpha=0.5$ , VF=20.

**Figure 4.1:** Some of the geometries described in **Table 4.1**. From left to right, top to bottom: d3,  $\alpha=0.2$ , VF=30; d1,  $\alpha=0.4$ , VF=30; d7,  $\alpha=0.6$ , VF=20; d4,  $\alpha=0.6$ , VF=30.

**Figure 4.3:** Range of permeability values for Optimized topologies and TPMS.

**Figure 4.4:** Range of Young's Modulus values for Optimized topologies and TPMS.

**Figure 4.5:** Range of FElast values for Optimized topologies and TPMS, for deformation field  $\varepsilon=[1,1,1,0,0,0]$ .

**Figure 4.6:** Range of FElast values for optimized topologies and TPMS, for deformation field  $\varepsilon=[0,0,0,1,1,1]$ .

**Figure 4.7:** FElast and permeability values for the TPMS and all Optimized geometries used in this section, for  $\varepsilon=[1,1,1,0,0,0]$ .

**Figure 4.8:** SD80 (left); resulting geometry of using the rigidity optimization problem using the aforementioned TPMS's porosity and permeability attributes as constraints (right). The black circles indicate one of the design differences.

**Figure 4.9:** Some of the optimized structures created under the permeability optimization problem to replicate properties of TPMS SD60 (left); SD70 (center); SD80 (right).

## List of Tables

**Table 3.1:** TPMS geometries used for comparison and their attributes.

**Table 4.1:** Properties of optimized topologies created using the multi-objective problem for the given  $\alpha$  values, initial solutions, VF, and for  $\epsilon=[1,1,1, 0,0,0]$ .

**Table 4.2:** Properties of optimized topologies created using the multi-objective problem for the given  $\alpha$  values, initial solutions, VF, and for  $\epsilon=[0,0,0,1,1,1]$ .

**Table 4.3:** Maximum deviations of values between TPMS and the optimized structures which used them as initial solutions.

**Table 4.4:** Attributes of nine geometries created from the same initial solution under the rigidity optimization problem. Constraint functions used the VF and FPerm of the respective TPMS.

**Table 4.5:** Attributes of 8 geometries created from the same initial solution under the permeability optimization problem. Constraint functions used the VF and FElast of the respective TPMS.

**Table 4.6:** Attributes of 3 optimized geometries created from the same initial solution under the multi-objective optimization problem.

**Table A1:** Attributes of TPMS and 18 geometries created from the same initial solution under the rigidity and permeability optimization problems. Constraint functions used the attributes of the respective TPMS. RO: rigidity optimization problem; PO: permeability optimization problem.





## Abbreviations and Symbols

$\nabla P$ : pressure gradient vector [Pa/m]

$\alpha$ : weight factor

$\Gamma_q$ : permeability problem boundary

$\Gamma_t$ : elasticity problem boundary

$\varepsilon$ : strain field

$\lambda^*$ : solution of the dual problem

$\mu$ : fluid viscosity [Ns/m<sup>2</sup>]

$\rho$ : density

$\rho^*$ : solution of the sub-problem

$\varphi$ : weight function

$\chi^m$ : microstructure pressure perturbations

$\bar{\chi}$ : deformation nodes

$\Omega_\varepsilon$ : scaffold domain

$b$ : body forces [N/m<sup>3</sup>]

BCP: biphasic calcium phosphate

BTE: bone tissue engineering

Ca: calcium

CAD: computer aided design

CaP: calcium phosphate

CFD: computational fluid dynamics

$d$ : microstructure size

$D$ : macroscopic domain size

$E$ : stiffness coefficients

$E_0$ : void stiffness

$E^H$ : homogenized stiffness

$f$ : fluid generated or removed per unit volume [s<sup>-1</sup>]

FDM: fused deposition modelling

FE: finite element

FElast: stiffness function

$F_i$ : constraint functions

$F_{obj}$ : objective function

FPerm: relative permeability function

HA: hydroxyapatite

$l_j$ : lower asymptote

K: permeability coefficients

$K_0$ : void permeability

$K^H$ : homogenized permeability

KKT: Karush-Kuhn-Tucker

Mg: magnesium

MMA: method of moving asymptotes

$p$ : penalization factor of SIMP model

P: pressure

PCL: poly(caprolactone)

PEG: poly(ethylene glycol)

PGA: poly(glycolic acid)

PLA: poly(lactic acid)

$q$ : Darcy flux vector [m/s]

$\bar{q}$  : Darcy flux on boundary  $\Gamma_q$  [m/s]

SD: Schwarz Diamond

SG: Gyroid

SIMP: solid isotropic material penalization

SLS: selective laser sintering

SP: Schwarz Primitive

Sr: strontium

STL: stereolithography

T: traction on boundary  $\Gamma_t$  [N/m<sup>2</sup>].

TCP: tricalcium phosphate

TPMS: triply periodical minimal surface

u: displacement field [m]

$u_i$ : upper asymptote

v: virtual displacement field

VF: volume fraction [%]

y: length scale of microstructure

Y: length scale of scaffold



# 1 Introduction

The term “tissue engineering” as it is understood today originated in a 1985 proposal by Y.C. Fung and his team (Viola et al., 2003). It became popularized some years later and described as “*an interdisciplinary field that applies the principles of engineering and the life sciences toward the development of biological substitutes that restore, maintain, or improve tissue function*” in Langer & Vacanti (1993). Nowadays, tissue engineering includes the creation and application of scaffolds, cell proliferation, cell substitutes, and many other areas with a lot of potential in order to simulate natural behavior (Chocholata et al., 2019). This work will focus on bone tissue engineering (BTE), the area of tissue engineering which addresses bone. Specifically, the focus will be on scaffolds used in BTE.

Bone comprises the majority of the skeletal system. It provides the mechanical functions of support, protection, and movement assistance, while additionally producing blood cells, aiding in mineral homeostasis, and storing fat. This is a hard mineralized tissue whose matrix is composed of 15% water, 30% collagen fibers, and 55% crystalized mineral salts, the most common of which is calcium phosphate (Tortora & Derrickson, 2016).

As described by Tortora & Derrickson (2016) and seen in **Figure 1.1**, there are two distinct types of bone tissue: cortical (or compact) and trabecular (also known as spongy or cancellous). Cortical bone is stronger and heavier, and makes up about 80% of the skeleton. It consists in repeating structural units, the osteons, made of concentric lamellae arranged around an osteonic canal. Trabecular bone is lighter and always found under cortical bone. It is composed by lamellae arranged irregularly in thin columns. Structure variety goes beyond these two types of bone, since this tissue undergoes constant remodeling, where osteoclasts remove material from the matrix and osteoblasts add to it, adapting the bone to the loads it is subjected to.

While bone can remodel and regenerate, due to its vital mechanical functions there are situations where a deformity or injury cannot be fully repaired naturally or easily enough within a small timeframe (in order to prevent further complications) (Stevens, 2008). In such situations it might be necessary to perform a bone graft, where some of the missing bone is replaced.

Traditional bone grafts consist of autografts, where bone is harvested from the patient's body itself, allografts, where bone is harvested from another body, and xenografts, where bone or an equivalent structure from a different species is used (Tortora & Derrickson, 2016).

Autografts are still considered by many as the gold standard (Stevens, 2008). The harvested bone can be reliably integrated into the host bone and there's a much smaller risk of the graft being rejected. The major drawbacks to this procedure are the lack of supply and the likelihood of donor site morbidity related to harvesting (Sohn & Oh, 2019). Allografts are commonly harvested from cadavers and while this prevents the main drawbacks present in autografts, they require rigorous processing to avoid disease transmission or rejection. Some of the properties of the tissue can be negatively impacted by this processing, leading to a poorer integration (Boyce et al., 1999). Xenografts, while initially considered a viable option, are now the least common type of graft and generally regarded as unsuitable due to the

risks of rejection, disease or virus transmission, poorer integration, and toxicity, among others (Porter et al., 2009) (Dumitrescu et al., 2021).

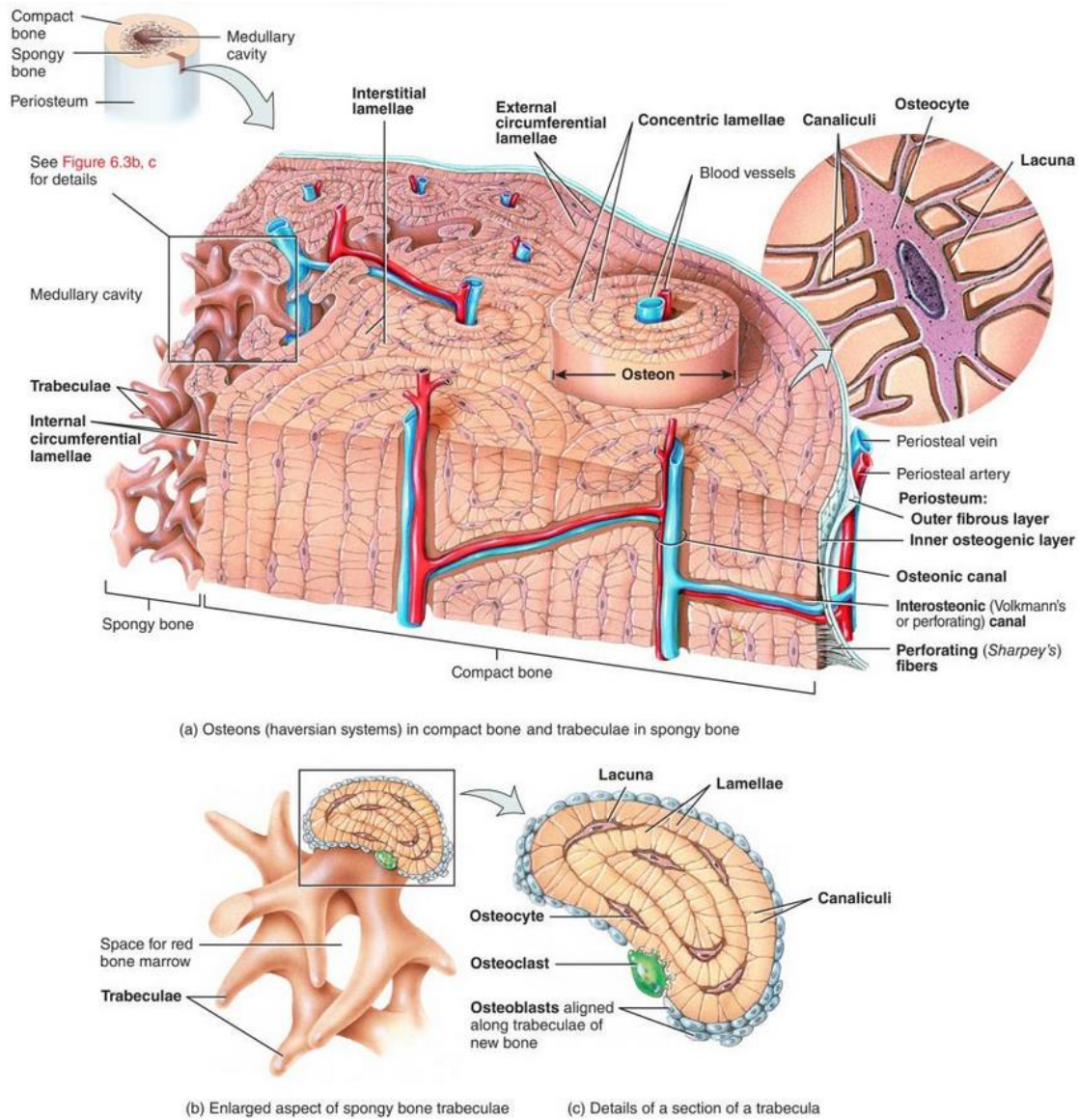


**Figure 1.1:** Structural details of bone tissue (Tortora & Derrickson, 2016).

To avoid the numerous drawbacks associated with the traditional bone grafting methods, the field of BTE has been researching the creation and application of scaffolds. These artificial bone substitutes are porous structures which provide support for cell seeding and proliferation. Different materials, geometries, and levels of porosity allow scaffolds to be used for cortical or trabecular bone and be well suited to the site of application. Regarding the internal geometry of scaffolds, triply periodic minimal surfaces (TPMS) have shown to be suitable in promoting tissue growth while providing the necessary mechanical support (Yoo, 2014). Optimized geometries focused on desired specifications are a

promising alternative (Sturm et al., 2010) (Zhou & Li, 2008). However, it is still not fully known which method of geometry creation is the most suitable for BTE.

## **1.1 Motivation and Objectives**

Encouraging viable alternatives to traditional bone grafts is the main motivator for this work. In order for scaffolds to be well suited for BTE applications, it is necessary to know how to create them so that required rigidity and permeability properties are achieved, among others. The chosen geometry is one of the main factors influencing these properties. While TPMS offer many possibilities in scaffold design, one must adapt and choose a type of TPMS for a problem at hand. Meanwhile, the process of optimization can create geometries tailored for the needed circumstance.

It is still yet unclear if any of these two methods is more advantageous overall, or shows more benefits for specific situations, and it is this what this work seeks to investigate. To do so, a pre-existing optimization tool used by Dias (2013) was updated and used to create a variety of geometries according to user inputs such as the problem type (which defines the properties to be maximized), material properties, applied strain field, cell model size, and stopping conditions. The porosity, as well as permeability and rigidity attributes of these were compared to those of TPMS under different scenarios. Additionally, TPMS were optimized with the optimization tool, and additional geometries based on the properties of TPMS were created, in order to understand if and where the TPMS used could be enhanced.

With the results obtained during this work, a better comprehension of the scope of use of optimized topologies in BTE should be obtained and observations made on what is currently lacking in optimization, when compared to other technologies.

## **1.2 Thesis Structure**

This thesis is divided into 5 sections: the introduction, literature review, methodology, results and discussion, and conclusions.

The introduction provides insight into the subject of BTE and bones themselves, as well as the motivation and aims of this work. Afterwards, the literature review section covers the requirements and practices of scaffold production. The common materials used, manufacturing techniques, and methods of creating geometries are explored. The methodology section then provides an explanation of the topology homogenization theory and how topology properties were calculated, and details how the optimization tool functions and which TPMS topologies were used. The results and discussion section showcases the computational results of this work: the properties and designs of various optimized topologies and the comparisons between these and TPMS geometries. In addition, they are analyzed and discussed in depth. Then, the conclusions regarding the efficiency of optimized and TPMS topologies are provided. Additionally, possible future research is discussed.

## 2 Literature Review

### 2.1 Scaffold Requirements

Scaffolds need to meet certain requirements to promote healthy bone growth while providing support. Porter et al. (2009) lists these requirements as:

- 1) temporarily providing mechanical support at the area of implantation,
- 2) serving as substrate,
- 3) being porous such that vascularization and bone in-growth are permitted,
- 4) encouraging bone cell migration into the scaffold,
- 5) encouraging and aiding osteoinduction,
- 6) enhancing osseointegration,
- 7) degrading in a controlled manner in order to keep developing bone supported,
- 8) not producing toxic degradation products,
- 9) not inciting a chronic inflammatory response,
- 10) being capable of sterilization without loss of bioactivity,
- 11) delivering bioactive molecules or drugs in a controlled manner.

It is necessary to point out that requirement 11, despite being of great benefit, is not strictly necessary in a scaffold. The remaining requirements, however, are mandatory for BTE applications.

The first requirement addresses the immediate need to substitute the missing bone's mechanical functions. If the scaffold's stiffness does not match the needs of the site of intervention, the new bone might not grow in the desired configuration, the healthy bone might be weakened, or the area could become unstable, leading to complications. Stiffness depends not only on the chosen material but also on the scaffold's geometry and a balance must be achieved between preventing scaffold failure and avoiding stress-shielding phenomena (Ryan et al., 2006).

Requirements 2 to 6 address the scaffold's bioactivity. A scaffold must allow vascularization and thus transport of nutrients and waste, and it should encourage cell migration and proliferation so that the new bone tissue is properly integrated. These factors are tied to the permeability of the scaffold which is heavily influenced by the geometry (Ali et al., 2020). Under the same porosity, a higher permeability with larger pores in the structure leads to a better flow of nutrients, but smaller pores enhance tissue growth by providing a higher surface area, at the cost of lower permeability and poorer vascularization (O'Brien et al., 2005). To avoid sacrificing any of these requirements, the pore size used for bone is typically between 200  $\mu\text{m}$  and 1 mm (Egan, 2019). However, if, despite being constrained by pore size, a scaffold has a very high permeability, its mechanical properties might be compromised, and the first requirement will not be met.

The seventh requirement also compromises stiffness since as the scaffold degrades, so will its mechanical properties. Because of this, it must degrade at a similar pace to that of bone formation, so that the new tissue will always be supported by the scaffold's mechanical strength, but its growth not impeded by the scaffold (Zhang et al., 2014).



Requirements 8 to 10 address biocompatibility and are tied mostly to material and production method. Foreign objects in the human body are prone to cause complications and special care must be had to avoid those. In addition to that, some scaffold topologies can lead to toxicity, since if any toxic product from the manufacturing process becomes trapped in pores with no interconnectivity, the body will be exposed to it as the scaffold degrades.

It is clear that a balance between stiffness and permeability must be found.

## **2.2 Scaffold Production**

To meet the requirements discussed in the previous section, scaffolds must be produced with special attention paid to their material, manufacturing technique, and internal structure. The following sections will explain these matters in more detail.

### **2.2.1 Materials**

In BTE, many materials have been considered for scaffold production. The most common are metals, ceramics, and polymers and usually a combination of these is used.

#### **2.2.1.1 Metal**

Titanium and its alloys have been commonly used to manufacture orthopedic devices, such as prosthesis and implants, given their low stiffness, high specific strength, and biological inertness (Dabrowski et al., 2010). These conventional implants are solid and known to cause stress shielding effects which can inhibit tissue regeneration and lead to further complications in the patient. Scaffolds made of these materials, however, have shown to be biocompatible and support osteogenesis (Lv et al., 2015). Their superior mechanical properties are beneficial in cases of slow bone growth but otherwise they can lead to stress-shielding, in addition to not degrading in a way that respects requirement 7 seen earlier. Moreover, metal scaffolds release ions over time which may cause toxicity and inflammatory responses (Turnbull et al., 2018).

#### **2.2.1.2 Ceramic**

Like metals, ceramic materials have been used extensively in prosthesis with success and are promising candidates for scaffold manufacturing. Their major appeal is the favorable biocompatibility and bioactivity, being less likely to cause inflammatory responses. Mechanically, they show high compressive strength, low friction, and high wear resistance, in addition to higher brittleness (Turnbull et al., 2018). While most of these are important and desirable properties for BTE, the degradation rates may not be favorable.

The most frequently used ceramic family in BTE is calcium phosphates (CaP), of which the most used are calcium hydroxyapatite (HA), tricalcium phosphate (TCP), and biphasic calcium phosphate (BCP), a composite of the previous two. CaPs are known to not only be biodegradable but also encourage osteoinductivity, facilitating integration with host tissue (LeGeros, 2002).

HA has a composition very similar to human bone mineral, and has proven to be biocompatible and bioactive. However, it is hard and brittle and has a slow degradation rate, making it unsuitable for use in BTE on its own. TCP is another biocompatible and bioactive bone substitute material that has been used for scaffold production with good results, having shown better tissue regeneration than HA (Chocholata et al., 2019). One of its major drawbacks is the too-fast degradation rate, which the development of BCP and bio-glasses has overcome with some success (Porter et al., 2009).

#### **2.2.1.3 Polymers**

Polymers are the most promising of these types of material. They are macromolecules composed of a large number of monomers connected by covalent bonds. Polymers have a benefit over the previous material types as they are easy to obtain and manufacture, are very versatile, and have tunable degradability. They can be classified according to their origin as natural or synthetic.

Among natural polymers we have polysaccharides (which include starch, alginate, chitosan, and hyaluronic acid derivatives) and proteins (which include soy, collagen, fibrin gels, and silk). These types of polymers possess some favorable properties such as biocompatibility, ductility, biodegradability, and often have molecules on their surfaces which enhance bioactivity. However, these polymers have suboptimal mechanical properties for BTE, suffer from a lack of tuneability of degradation rates, and may contain pathogenic impurities (Liu & Ma, 2004).

The synthetic polymers which have been used in BTE include poly(lactic acid) (PLA), poly(glycolic acid) (PGA), poly(caprolactone) (PCL), poly(ethylene glycol) (PEG), and some of their copolymers. Unlike natural polymers, their degradation rate can be controlled and they have better mechanical properties but poorer innate bioactivity.

Overall, synthetic and natural polymers possess low elastic moduli when compared to other material types and cannot meet the mechanical requirements of BTE when used on their own (Turnbull et al., 2018).

#### **2.2.1.4 Composite Materials**

Given the advantages and disadvantages of all these materials in mind, scaffolds of a single material would be unable to fully replicate the properties of bone. Because of this, combining multiple materials with favorable properties is considered the better approach (Chocholata et al., 2019). These scaffolds generally include a polymer phase with good mechanical properties and an inorganic phase with bioactivity.

Alloys of Magnesium (Mg) are considered as the most promising biodegradable metals. Alloys resulting from the combination of Mg and nutrient elements such as calcium (Ca) and strontium (Sr) have been recommended for future clinical application as per Jiang et al. (2018), specifically Mg-1Sr, Mg-1Ca-0.5Sr and Mg-1Ca-1Sr alloys. Ternary MgCaSr alloys generally show enhanced cell adhesion when compared to binary MgSr alloys, whereas these latter also have some of the lowest degradation rates.

Composites of HA, Sr, and chitosan have additionally shown good cell proliferation and osteogenic differentiation, as well as composites of nickel-titanium treated with sodium hydroxide, porous 3D

injected iron-magnesium scaffolds, composite titanium-silica scaffolds with complex geometry and stainless steel, titanium and cobalt chromium alloys, and other composites.

With so many possibilities available with different advantages and disadvantages to each, material choice in scaffold production for BTE is a debated matter still under research.

## 2.2.2 Manufacturing Techniques

Scaffolds have been produced using a large variety of techniques, and sometimes combinations of them. Some materials can only be used with specific techniques, and each has its own benefits. Turnbull et al. (2018) lists the main scaffold manufacturing techniques as solvent casting, particulate leaching, gas foaming, emulsification freeze-drying, phase separation, electrospinning, and various 3D printing and 3D bioprinting techniques. In this section they'll be explained in some detail.

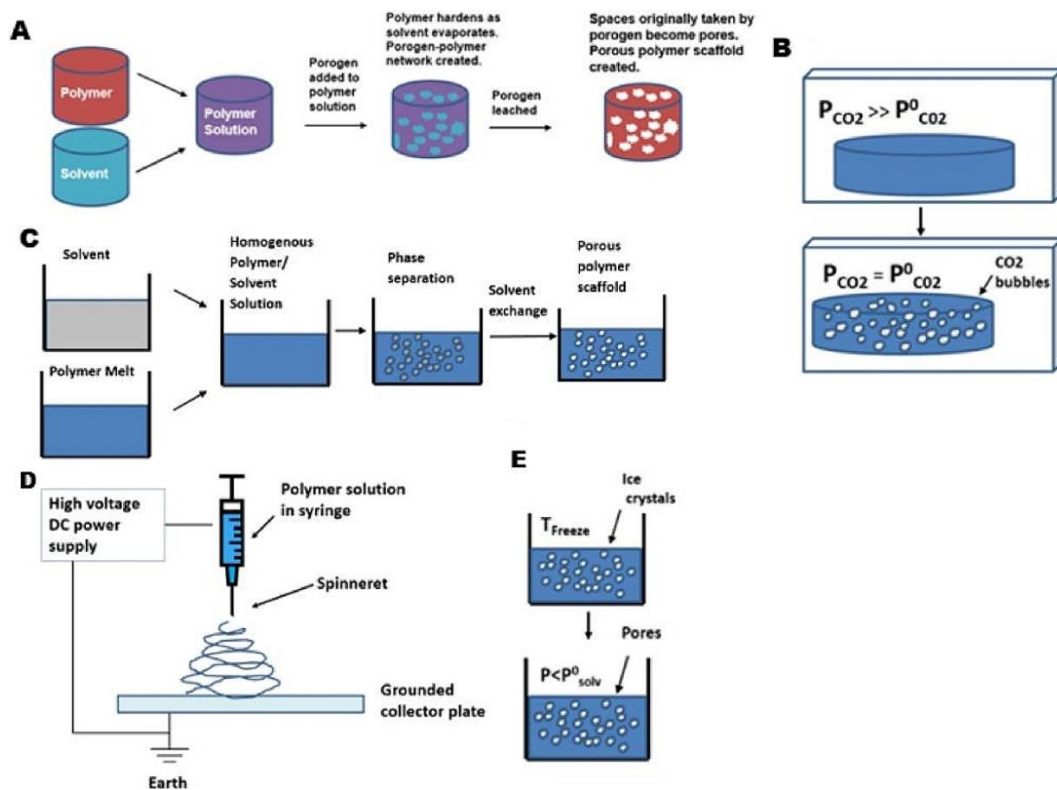


**Figure 2.1:** Common scaffold fabrication techniques. A: solvent casting-particle leaching process; B: gas foaming; C: phase separation; D: electrospinning; E: freeze-drying. Adapted from Turnbull et al. (2018).

### 2.2.2.1 Solvent Casting and Particulate Leaching

This is the most common and simple technique, as it does not require any special equipment (Chocholata et al., 2019). Solvent casting and particulate leaching consists in dissolving a polymer in an organic solvent, mixing it with a water-soluble porogen, such as salt, and casting the resulting mixture into a mold. The solvent evaporates and the polymer/porogen hardens, and afterwards water is used to

dissolve the porogen, leaving behind the final hardened polymer scaffold. The amount of porogen affects the porosity of the scaffold, and the crystal size affects pore size. Unfortunately, the pore shape and interconnectivity are difficult to control with this technique, the thickness and mechanical properties of the scaffolds are limited (Turnbull et al., 2018).

#### **2.2.2.2 Gas Foaming**

The gas foaming technique uses gas expansion of bubbles inside a polymer to create the pores. Carbon dioxide is used as it is a common, low-toxicity, non-flammable gas. While this technique allows for highly porous scaffolds, the permeability is low due to lack of pore interconnection, especially at surface level.

More permeable scaffolds can be produced by using the gas foaming/salt leaching method. A combination of ammonium bicarbonate salt and acid substances at increased temperatures causes ammonia and carbon dioxide to be released as gases. This leads to macroporous structures with interconnected pores where cells can be seeded with high viability (Chocholata et al., 2019).

#### **2.2.2.3 Emulsification Freeze-Drying**

This technique employs phase separation. An emulsion is prepared by homogenization of a polymer in an organic solvent and water. This emulsion is rapidly cooled down and liquid phases are removed by freeze-drying. The resulting scaffolds are highly porous, but often this porosity is irregular, on top of the pore size being small. Additionally, this technique has a long processing time.

#### **2.2.2.4 Phase Separation**

Phase separation uses changes in thermal energy to induce the de-mixing of a homogenous polymer/solvent solution. A polymer is dissolved in a high-boiling, low molecular weight solvent at high temperature, around the melting point of the polymer. This allows a homogenous melt-blend to be formed, which is then cast into a desired scaffold shape, and cooled in a controlled manner to induce phase separation and precipitation of the solution into a polymer-rich phase and a solvent-rich phase. The solvent in the solvent-rich phase is then removed through extraction, evaporation, or sublimation, leaving behind a porous scaffold.

This process originates scaffolds with a pore size too small for cell seeding and growth in BTE, leading to a coarsening process being required.

#### **2.2.2.5 Electrospinning**

Electrospinning is a commonly used manufacturing technique which uses an externally applied electric field to draw charged threads of polymer solutions or melts as thin jets from a capillary tube towards a collector plate. Submicrometric fibers are created and deposited sequentially to create a scaffold. The thickness of the fibers can be controlled by type and concentration of the polymer and through the setting of the electrospinning device. Additionally, this method allows the inclusion of composite materials and biomolecules in the scaffold.

Given the instability of natural polymers and harmful degradation products of synthetic polymers, a combination of these is generally used.

### 2.2.2.6 3D Printing

The previously discussed production methods suffer from limited control over the scaffold's final properties, and the emergence of 3D printing techniques came to overcome many of these limitations. 3D printing creates structures by processing a material substrate from the bottom in layers, so that each new layer adheres to the previous one, following the structure of a computer-aided design (CAD) model. In this section, some of the more common 3D printing techniques used in BTE will be explored.

Stereolithography (STL) was one of the earliest forms of 3D printing to be developed. It consists on a directed UV laser, used to polymerize a liquid UV-curable photopolymer resin in layers, as the printing platform moves down with each new layer. The resin not touched by the laser remains liquid, thus covering the solid polymer as it moves down, so that a new layer can be cured. At the end, the excess resin is removed from the structure, which is then further cured in an oven and subjected to surface treatment.

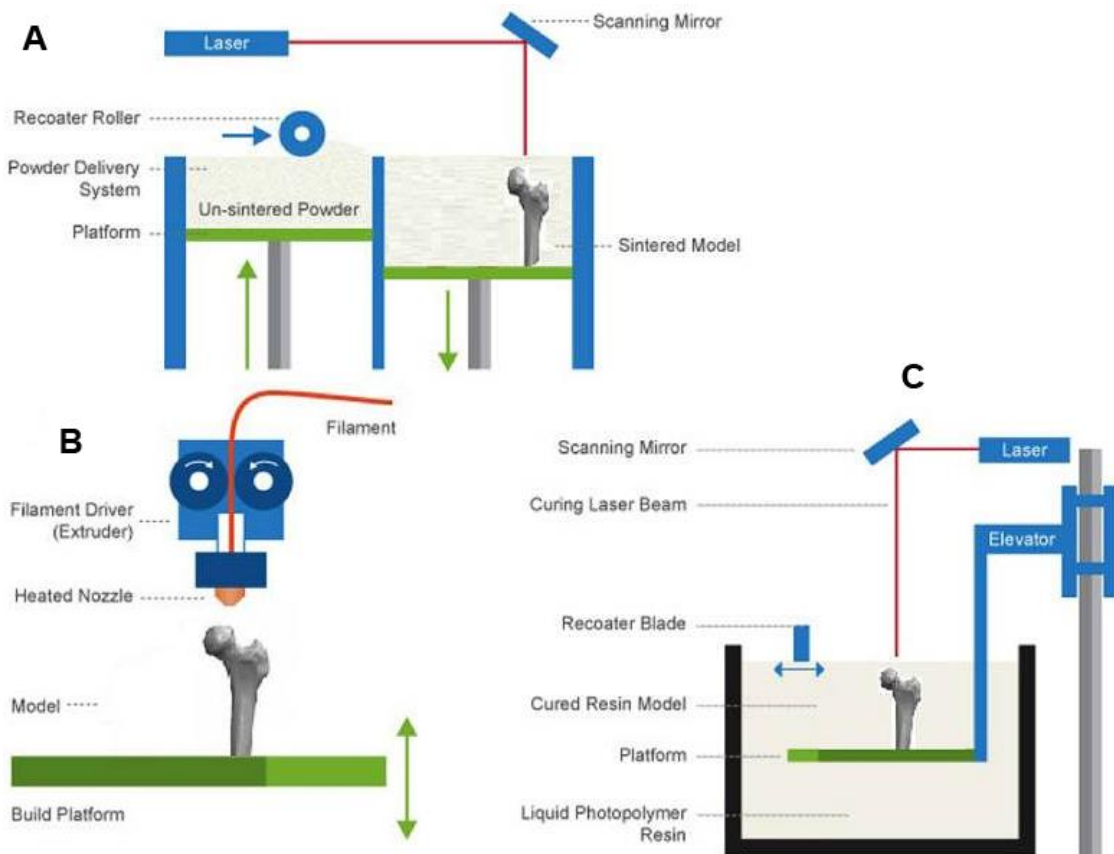


**Figure 2.2:** Common 3D printing techniques. A: selective laser sintering; B: fused deposition modelling; C: stereolithography. Adapted from Turnbull et al. (2018).

This is a quick method of producing scaffolds with a controlled structure and high resolution, but it is costly and the choice of materials restrained.

Fused deposition modelling (FDM) uses a printhead with adjustable temperature to deposit melted thermoplastic material onto a platform in layers. The molten filaments quickly cool after being laid out in

the structure, creating a scaffold. This method can create highly porous and permeable structures with good mechanical properties and without requiring a solvent removal stage. The high temperatures, however, limit the choice of materials and the pores may not have a consistent shape and size.

Selective laser sintering (SLS) consists in using a computer controlled laser beam to fuse a powder in stacked layers, sintering it together into a solid structure. This method can successfully create complex structures of a wide choice of materials and allows control over pore size and porosity, within some limits. The material choice or the limitations of the printer used have been shown to create scaffolds with slight deviations from the CAD models, which may lead to poorer mechanical properties (Dias et al., 2014) (Williams et al., 2005).

### 2.2.2.7 3D Bioprinting

3D bioprinting is an emerging technology which builds upon the already-existing 3D printing techniques. The various methods of scaffold manufacturing explored previously require posterior cell seeding onto the created scaffolds, limiting the ability to create complex tissue constructs. Bioprinting overcomes that by depositing living cells and other biomaterials during the printing process. The more commonly used bioprinting methods will be explored in this section.

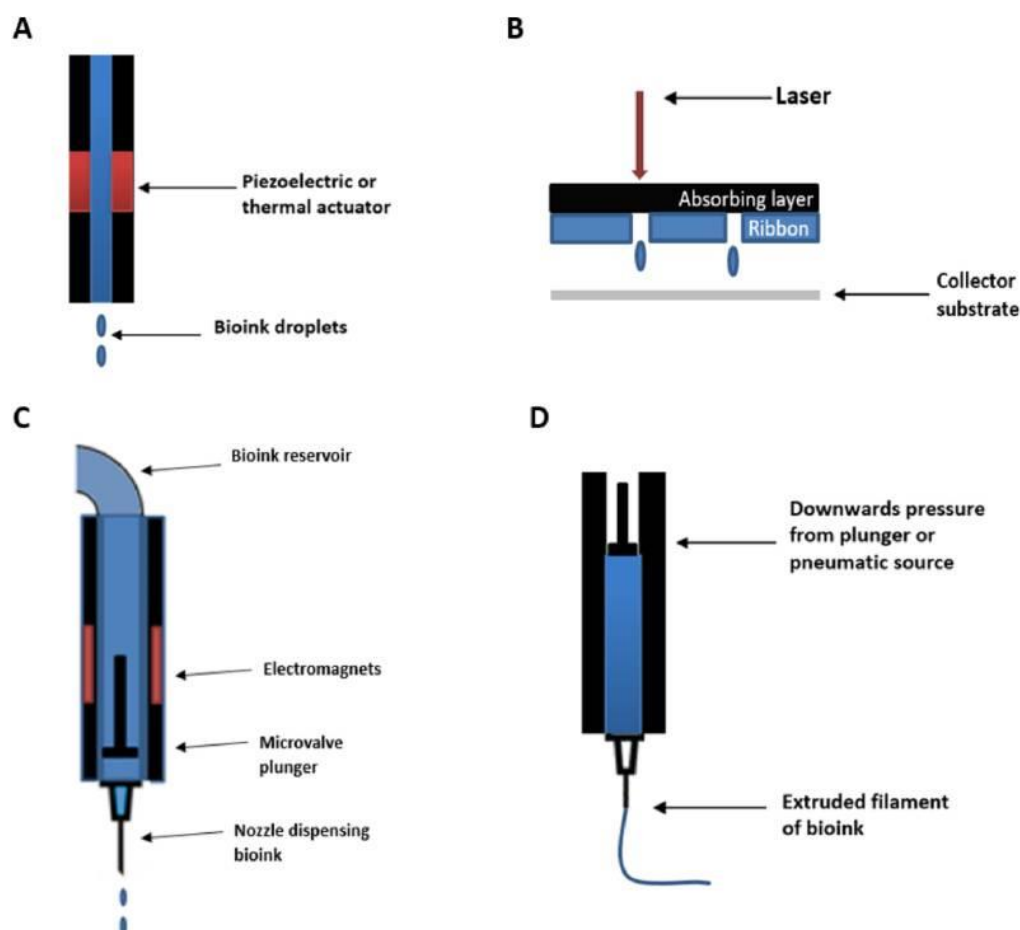


**Figure 2.3:** Common bioprinting techniques. A: inkjet bioprinting; B: laser-assisted; C: microvalve; D: extrusion bioprinting (Turnbull et al., 2018).

Inkjet bioprinting, also known as drop-on-demand bioprinting, is a method in which thermal or acoustic forces are used to eject droplets of bioink from a pint head nozzle. Because this technology is adapted from desktop inkjet printers, it is affordable, widely available, and contains high printing speed. Its major drawbacks are the nonuniform droplet sizes, frequent nozzle clogging, the risk of exposing materials to thermal and mechanical stress, and the low viscosity of the bioink, which leads to an additional step of gelation or crosslinking being required.

Laser-assisted bioprinting consists in using a pulsed laser beam to generate a high-pressure bubble, which propels cell-containing materials from an initial print ribbon to a collector substrate. Despite some promising applications, this method is expensive, time consuming and can cause thermal damage to the cells.

Microvalve bioprinting is a technique where pressurized bioink is dispensed from cartridge tips through opening and closing a small valve. This allows for cells to be printed with high viability and functionality, and for other biomaterials such as collagen to be deposited.

Extrusion bioprinting involves deposition of continuous filaments of material, unlike the previous methods. A syringe is put under mechanical or pneumatical pressure in order to make bioink extrude through a nozzle. This allows for very high cell densities to be deposited. Some of the potential drawbacks of this method are the lower printing resolution and damage to the cells due to shear stress.

### **2.2.3 Geometry**

Not every manufacturing method allows good control over the final geometry of the scaffold. More conventional methods such as solvent casting, particulate leaching, gas foaming, emulsification freeze-drying, phase separation, and electrospinning only allow for moderate control of the topology, such as the pore density, connectivity, or size. 3D printing and bioprinting methods, however, print 3D structures following CAD models, allowing for a precise control of the manufactured scaffold's geometry (Egan, 2019). Thus, careful consideration must be had when designing the geometry of a CAD model as it will greatly impact mechanical properties, permeability, bioactivity, and biocompatibility (Zadpoor, 2015). When it comes to designing CAD models, the common approach used is to design a unit cell and use it as a pattern for a lattice structure (Rosso et al., 2019) (Kladovasilakis et al., 2021) (Habib et al., 2016) (Egan et al., 2017). Depending on the desired properties of the scaffold as well as the materials and manufacturing method to be used, the unit cell can be a strut-like design, a TPMS, or an optimized geometry. This work will focus on the latter two options.

#### **2.2.3.1 TPMS**

TPMS are surfaces defined by zero mean curvature and local area minimization, meaning that any sufficiently small cut taken from them has the smallest area among all patches created under the same boundaries (Torquato & Donev, 2004). These surfaces divide into continuous phases, which makes it possible to create structures with continuous and interconnected reinforcements.

Abueidda et al. (2019) describes structures composed of TPMS as having shown enhanced mechanical properties, especially regarding energy absorption, as well as higher surface-to-volume ratio. This higher surface-to-volume can greatly improve the bioactivity of the scaffold, as it allows better cell adhesion, migration, and proliferation (Yoo, 2014).

There are many types of TPMS designs, each with its own properties, but this work will only focus on the Gyroid (SG), Schwarz Diamond (SD), and Schwarz Primitive (SP) types (see **Figure 2.4**). Maskery et al. (2018) describes SP structures as having much higher elastic moduli than the other 2 types, at the cost of highly localized plastic deformation, buckling, and low failure strain, due to their high variation in load-bearing area. They recommend that SP types are more suited to scenarios which require high stiffness and strength in one loading direction, while SG and SD types are better suited to scenarios requiring a high strain before failure occurs.



**Figure 2.4:** TPMS structures. Right: unit cells of Gyroid, Schwarz D, and Schwarz P TPMS types, adapted from Kladovasilakis et al. (2021). Left: a printed scaffold composed of Schwarz P cells.

Scaffolds with TPMS geometries have been able to obtain mechanical properties similar to that of bone and numerical simulation has considered them suited for further testing in BTE applications, but clinical verification of their viability is still lacking (Castro, et al., 2020) (Castro et al., 2019) (Shi et al., 2018).

### 2.2.3.2 Topology optimization

TPMS architectures have many benefits and are, to a degree, versatile: one can choose among many types of TPMS and even modify parameters such as pore size to obtain multiple variations of a single TPMS type. However, only by studying the attributes of the final TPMS geometry is it possible to know if it meets the mechanical requirements of the implantation site and the permeability requirements for bioactivity (Dong & Zhao, 2021) (Castro, et al., 2020). As such, and given that scaffolds lend themselves well to optimal structural design problems due to their microstructure, research has been done in order to use computer models to create optimized scaffold structures (Bendsøe & Sigmund, 2004).

Olhoff & Taylor (1983) described structural optimization as “the rational establishment of a structural design that is the best of all possible designs within a prescribed objective and a given set of geometrical and/or behavioral limitations”. Structural optimization problems require three main components: the objective function, the design variables, and the state variables. The objective function defines the chosen problem and returns a value for each state, which is to be minimized or maximized in an optimal solution. It can measure, for example, permeability properties, volume, costs, etc. The design variables are functions describing the design, such as its boundary shapes, the number of connected nodes, or



load distributions. The state variables describe the state in respect to mechanical properties, permeability properties, velocity, temperature, etc. (Olhoff & Taylor, 1983) (Ghattas & Orozco, 1997).

Structural optimization problems can be separated into sizing, shape, and topology optimization problems. Sizing optimization problems address issues such as finding the optimal member areas in a truss structure, and their design model domain and state variables are already known and fixed. Shape optimization problems address issues such as finding the optimal shape for a domain. Topology optimization problems address issues such as finding the quantity, shape, and location of the material in the domain, in a manner much like architect Robert le Ricolais's quote: "The art of structure is where to put the holes" (Bendsøe & Sigmund, 2004).

Topology optimization as a material distribution problem was first introduced by Bendsøe & Kikuchi (1988), who demonstrated that with a suitable material distribution, optimal shapes could be provided for a mechanical problem, within given volume constraints. Since then, extensive research has been done on studying and enhancing topology optimization and it has shown great potential for use in BTE scaffold design.

Lin et al. (2004) demonstrated that topology optimization applied to bone scaffold design can reach properties comparable or better than those of conventional designs, with reduced stress shielding and deformation. Additionally, they remarked that topology optimization could tailor designs not just for the mechanical requirements of the implantation site, but also for the materials chosen.

There's further research reinforcing the fact that optimization allows for the creation of different scaffold topologies specifically tailored for different mechanical applications. By maximizing permeability properties while placing constraints on mechanical properties, one can ensure that the best diffusion properties are obtained for the given mechanical requirements (Dias et al., 2014). Otherwise, other optimization models which don't focus on solely maximizing permeability or mechanical properties can be used. Boccaccio et al. (2018) implemented a mechanobiology-based optimization algorithm and the resulting topologies were found to lead to a predicted bone growth consistent with what is seen in *in vitro* studies. Additional promising optimization algorithms, such as the level-set method for topology optimization of steady-state Navier–Stokes flow by Zhou & Li (2008), have also been explored. A variety of options such as these can greatly aid in the process of finding the scaffold geometry best suited not only for the implantation site, but also for the materials and manufacturing methods to be used (Bahraminasab, 2020).

Castilho et al. (2017) employed topology optimization in the creation of a biodegradable implant for tibial tuberosity advancement and were able to demonstrate that it was possible to measure the mechanical requirements of the scaffold's implantation site and create a topology specifically designed for such parameters, meeting mechanical requisites while maximizing porosity. A scaffold optimized for mechanical properties was produced by Lin et al. (2007) and also shown to have favorable properties for possible BTE applications in the future.

### 3 Methodology

The optimization tool described by Dias (2013) was adapted for this work and used to create various scaffold topologies which were then compared with TPMS geometries. This section will cover the homogenization method used to calculate the scaffolds' properties, as well as how each of the properties were measured. Additionally, the development and functioning of the topology optimization tool is explained, followed by the choice of TPMS topologies used.

#### 3.1 Homogenization Theory

When a material topology is complex and has a high number of heterogeneities, such as in porous materials, computational methods are unable to take into account the entirety of the topology with all its parts and respective properties to calculate its properties. A simple elasticity problem becomes a problem with too many degrees of freedom requiring a vast amount of memory space and a prohibitive amount of time to compute. To surpass this issue, several methods of homogenization have been developed, where the complex heterogenous domain is substituted by another with the homogenized properties of the original. To do so, one must assume the complex domain is composed locally of repeated microstructures, or cells, and that the domain properties are periodic functions of the microscopic variable, where this periodicity is much smaller than that of the macroscopic variable. If the cell is considered to be of size zero, the computation of equivalent material properties by a limiting process becomes possible (Guedes & Kikuchi, 1990) (Bendsøe & Kikuchi, 1988).

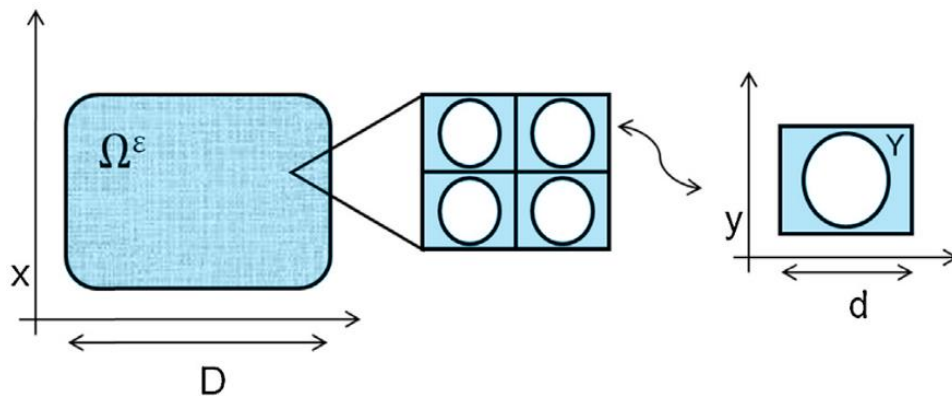


**Figure 3.1:** Scheme of the homogenization method. Left: domain of the scaffold  $\Omega^\varepsilon$ ; center: detail of the domain; right: unit cell  $Y$ .  $d$  is the characteristic length scale of the microstructure size, represented by  $y$ ;  $D$  is the characteristic length scale of the scaffold, represented by  $Y$ . Adapted from Dias et al. (2014).

To apply a homogenization approach, three assumptions must be made about the problem: periodicity, uniformity, and scale separation. In other words, the domain heterogeneities must be periodically distributed, so that all the corresponding domain properties are also periodic; the macroscopic fields must be uniform for all the microscopic representative volumes of the macroscopic domain; and the

characteristic length scale of the microstructure size ( $d$ ) should be much smaller than that of the macroscopic domain ( $D$ ), as shown in **Figure 3.1**.

The scaffolds in this work have a periodic microstructure of repeated cells, making the homogenization method an obvious and simple means to calculate their mechanical and permeability properties. Thus, homogenization was used in this work to calculate the equivalent elastic and permeability properties of geometries. The following sections 3.1.1 and 3.1.2 cover how the homogenized coefficients were calculated, following the method described by Guedes & Kikuchi (1990) and previously used by Dias (2013), Dias et al. (2014), and Coelho (2009).

### 3.1.1 Elasticity Homogenization

To calculate the elasticity coefficients, the general elasticity problem of **Figure 3.2** must be considered in its integral form.

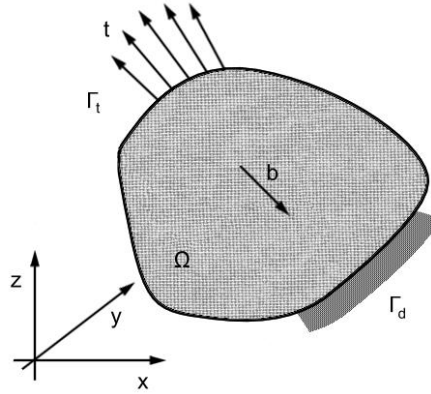


**Figure 3.2:** General elasticity problem.

With  $\mathbf{E}$  as the fourth order tensor of elastic coefficients (Pa),  $\mathbf{u}$  as the displacement field (m),  $\mathbf{v}$  as the virtual displacement field,  $\mathbf{b}$  the forces of the body ( $\text{N/m}^3$ ), and  $\mathbf{t}$  as the traction on the boundary  $\Gamma_t$  ( $\text{N/m}^2$ ), we can have:

$$\int_{\Omega} E_{ijklm} \frac{\partial u_k}{\partial x_m} \frac{\partial v_i}{\partial x_j} d\Omega = \int_{\Omega} b_i v_i d\Omega + \int_{\Gamma_t} t_i v_i d\Gamma, \quad \forall v \text{ admissible} \quad (3-1)$$

Following “upscaling”, the elastic coefficients are obtained through:

$$E_{ijklm}^H = \frac{1}{|Y|} \int_Y E_{pqrs} \left( \delta_{rk} \delta_{sm} - \frac{\partial \bar{\chi}_r^{km}}{\partial y_s} \right) \left( \delta_{pi} \delta_{qj} - \frac{\partial \bar{\chi}_p^{ij}}{\partial y_q} \right) dY \quad (3-2)$$

Here  $E^H$  are the homogenized elastic coefficients and the  $\bar{\chi}$  functions represent deformation modes for a unit cell subject to 6 unit average strains, 3 shear strains and 3 normal strains, given by the solutions of the series of problems in the microstructure (Guedes & Kikuchi, 1990).

### 3.1.2 Permeability Homogenization

To calculate a homogenized permeability, a method based on Darcy's Law was used. Darcy's law describes fluid flow through a porous medium (Neuman, 1977) and can be written as:

$$\mathbf{q} = -\frac{\mathbf{K}}{\mu} \nabla P \quad (3-3)$$

In which  $\mathbf{q}$  is the Darcy flux vector (m/s),  $\mathbf{K}$  is the second order tensor of the permeability coefficients ( $\text{m}^2$ ),  $\mu$  the fluid viscosity ( $\text{Ns/m}^2$ ), and  $\nabla P$  is the pressure gradient vector ( $\text{Pa/m}$ ).

Taking into account the rate of transfer per unit area  $\mathbf{q}$ , and the rate at which fluid is generated or removed per unit volume  $\mathbf{f}$  ( $\text{s}^{-1}$ ), as represented in **Figure 3.3**, for steady-state flow the balance of mass or continuity requirement gives:

$$\begin{aligned} \nabla^T \mathbf{q} - \mathbf{f} &= 0, & x \in \Omega \\ n^T \mathbf{q} &= \bar{q}, & x \in \Gamma_q \\ P &= P^* \text{ in } \Gamma_p \end{aligned} \quad (3-4)$$

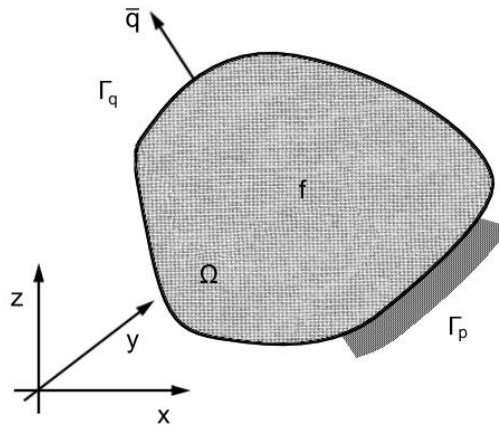


**Figure 3.3:** General flow problem.

Where  $\mathbf{q}$  is given by Equation (3-3) and  $\bar{q}$  is the Darcy flux on the boundary  $\Gamma_q$  (m/s). By describing the same fluid flow problem by a second order differential equation in  $P$ , obtained by combining Darcy's law and the balance of steady state flow, the permeability properties can be computed (Guedes & Kikuchi, 1990) (Dias et al., 2014). The integral form of this problem is:

$$\int_{\Omega} K_{ij} \frac{\partial P}{\partial x_j} \frac{\partial \varphi}{\partial x_i} d\Omega - \int_{\Omega} \varphi f \mu d\Omega - \int_{\Gamma_q} \bar{q} \varphi \mu d\Gamma = 0, \quad \forall \varphi \text{ admissible} \quad (3-5)$$

Where  $\varphi$  is an admissible arbitrary smooth weight function. By “upscaling” the problem defined in Equation (3-5), the homogenization method converts the domain into a homogenized equivalent one, where its equivalent permeability coefficients are obtained through:

$$K_{im}^H = \frac{1}{|Y|} \int_Y K_{ij} \left( \delta_{jm} - \frac{\partial \chi^m}{\partial y_j} \right) dY \quad (3-6)$$

Here the  $\chi^m$  functions represent the microstructure pressure perturbations for a unit average pressure gradient in each direction  $m$ .  $K_{im}^H$  is a matrix representing the homogenized coefficients of permeability, given by an average of the coefficients on the microstructure domain volume  $|Y|$ , weighted by  $\chi^m$ . This reflects the influence of the microstructure, implying that the permeability will depend on both the VF and the material distribution, i.e. two scaffolds with the same VF and different microstructures can have different permeability properties.

### 3.2 Optimization Tool

The optimization tool used in this work is an updated and improved version of the one described by Dias (2013). Originally written in FORTRAN 77, it was converted to Fortran 90 to facilitate memory allocation and future alterations. Many of the user given inputs were altered, preventing redundancy, adding more control over the chosen problem, and removing the need to recompile the program whenever certain inputs needed to be changed. Outputs were made easier to read and identify.

This optimization obtains geometries for unit cells by solving topology optimization problems in which it must define whether there is material or not at each point of the microstructure domain. For this, the material density  $\rho$  is used as a variable field and its maximum (1) and minimum (0) values correspond to solid and void material, respectively.

While other mesh sizes can be used, for this work all cells were defined by 20x20x20 models of 8-node cuboid elements.

#### 3.2.1 User Variables

The topology optimization tool requires a series of user-given parameters to be given so that the problem to be solved is described in detail. This includes information such as an initial geometry, which the tool will optimize, stopping conditions, cell size, strain field, and others such as problem type and applicable constraint functions, which will be explained further on.

Because the optimization process requires an initial geometry or solution to start from, a series of initial solutions were made, composed of an assortment of intermediary values between 0 and 1. These can be seen in **Figure 3.4**, with d6, d7, and d8 having been previously used by Dias (2013). To prevent rigid body movements, the optimization tool requires the number of a node which is to be fixed as a user input. In the initial solution, the elements connected to this fixed node must have a high density, thus being more rigid. Node 1, a vertex, was generally chosen for this purpose. Additionally, the initial solutions' elements cannot all have the same  $\rho$ , for if they are homogenized like this, it will not be possible to calculate gradients which allow an optimal solution to be found.

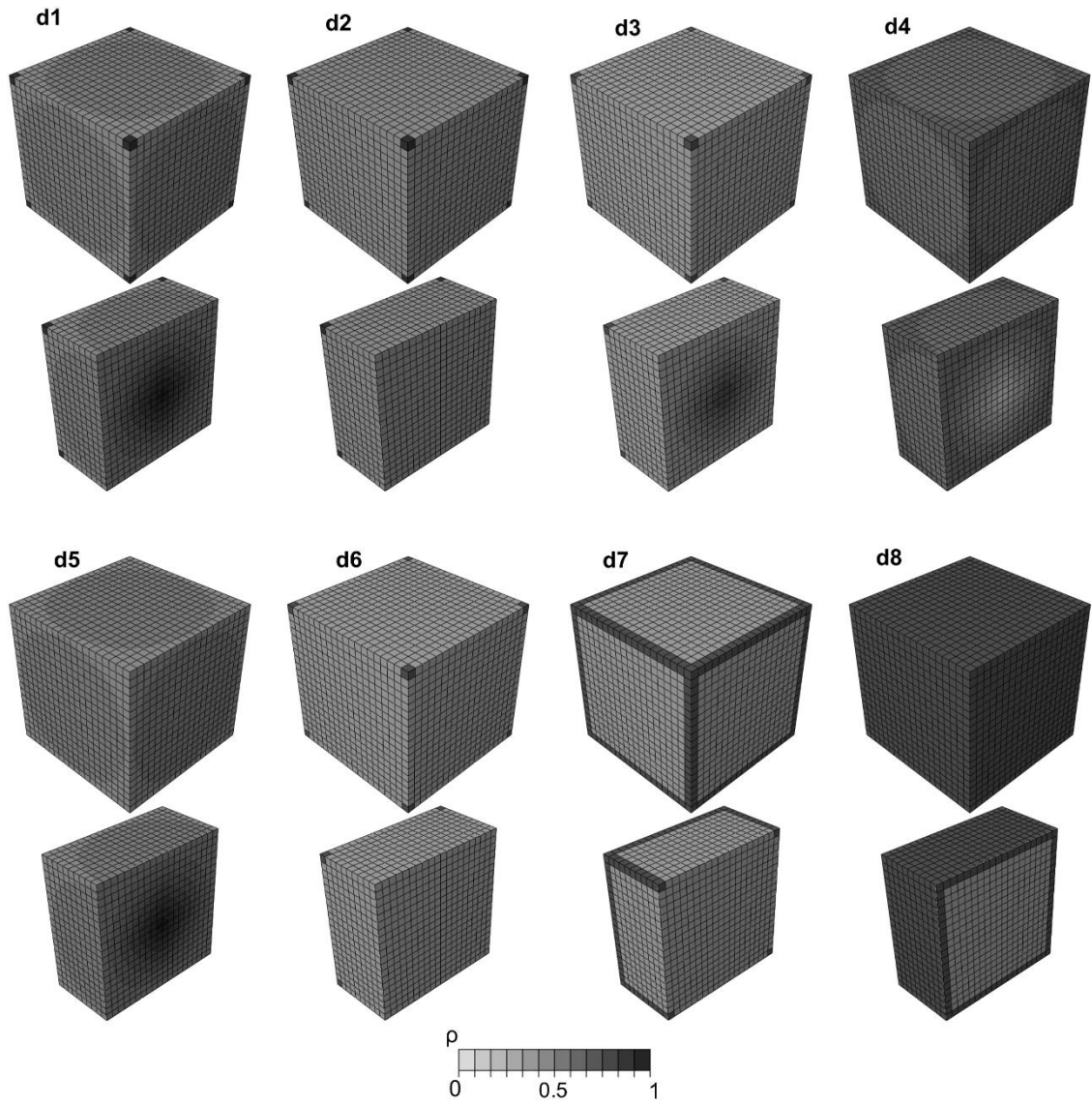


**Figure 3.4:** Initial solutions d1 to d8 used in this work.

Regarding stopping conditions, a maximum number of iterations and a convergence criterion must be chosen. The maximum number of iterations used throughout this work was 200, ensuring that if the optimization tool failed to find an optimal solution after that number of iterations, it would stop the optimization process and present the current solution. The convergence criterion is used to define when an optimal solution was reached, by checking if some of the parameters of the current solution have a small enough difference from the ones of the previous solution. The value used for this criterion in this work was  $1 \times 10^{-8}$ .

Another important aspect to define in this work is the strain field  $\epsilon$ , which is defined as a vector. This work only used triaxial normal and shear strains, respectively  $\epsilon=[1,1,1,0,0,0]$  and  $\epsilon=[0,0,0,1,1,1]$ .

### 3.2.2 Attribute Calculation

Several properties of the cells were calculated to compare which ones would be more suitable for scaffolds. In this section, these properties are defined and their means of calculation shown in detail.

#### 3.2.2.1 Volume Fraction and Porosity

Volume fraction (VF) is the percentage of the scaffold containing solid material while, inversely, porosity is calculated as the percentage of the scaffold composed of empty space.

With cell models composed of 20x20x20 cubic elements, VF is calculated as:

$$VF = \frac{\sum(\rho \text{ across all cells})}{8000} \quad (3-7)$$

Where  $\rho$  is the density of the material, between 1 and 0. Given that the finalized topologies in this work are composed of only solid material and empty space (meaning  $\rho$  can only be 1 or 0 at any point of the scaffold), these two attributes are related by:

$$Porosity = 1 - VF \quad (3-8)$$

#### 3.2.2.2 Relative Permeability

The relative permeability (FPerm) of a scaffold was then defined as the average of the homogenized coefficients on the main directions, and calculated by:

$$FPerm = \frac{K_{11}^H + K_{22}^H + K_{33}^H}{3} \quad (3-9)$$

FPerm is a relative value which can go from 0 (in the case of a completely solid cell) to 1 (when the cell is completely void).

#### 3.2.2.3 Stiffness FElast

The stiffness of a scaffold is then calculated by:

$$FElast = \frac{\varepsilon E^H \varepsilon}{2} \quad (3-10)$$

Where  $E^H$  are the homogenized elastic coefficients, and  $\varepsilon$  is a given strain field.

### 3.2.3 Problem Formulation

The density field describing the scaffold's microstructure will be the solution of the topology optimization problem described generally as:

$$\begin{aligned} & \text{minimize } F_{obj} \\ & \text{subject to } F_i(\rho) \leq F_i^*, \quad i = 1, \dots, m \\ & 0 \leq \rho \leq 1 \end{aligned} \quad (3-11)$$

Where  $F_{obj}$  is the objective function and  $F_i$  are the constraint functions. This objective function can be defined in multiple ways depending on the goal of the problem, which can be the maximization of a

property or multiple weighted properties. The constraint functions depend on this goal as well, guaranteeing specific values of properties or imposing minimum or maximum values on them.

Generally, the solution of an optimization problem is based on the resolution of the necessary optimal conditions of Karush-Kuhn-Tucker (KKT) (Coelho, 2009). These can be obtained from the stationarity of the augmented Lagrangean function which is associated to the optimization problem. In this work, the gradient of the objective and constraint functions depend on the gradients of FPerm, FElast, and/or VF. The gradient of the former two is then based on the gradient of the homogenized properties (Bendsøe & Sigmund, 2004):

$$\left\langle \frac{\partial K_{ij}^H}{\partial \rho}, \delta \rho \right\rangle = \frac{1}{|Y|} \int_Y \frac{\partial K_{sm}^H}{\partial \rho} \left[ \delta_{is} - \frac{\partial \chi^i}{\partial y_s} \right] \left[ \delta_{jm} - \frac{\partial \chi^j}{\partial y_m} \right] \delta \rho \, dY \quad (3-12)$$

$$\left\langle \frac{\partial E_{ijkl}^H}{\partial \rho}, \delta \rho \right\rangle = \frac{1}{|Y|} \int_Y \frac{\partial E_{hsmq}^H}{\partial \rho} \left[ \delta_{km} \delta_{lq} - \frac{\partial \bar{\chi}_m^{kl}}{\partial y_q} \right] \left[ \delta_{ih} \delta_{js} - \frac{\partial \bar{\chi}_h^{ij}}{\partial y_s} \right] \delta \rho \, dY \quad (3-13)$$

A finite element (FE) procedure was used to solve the elasticity and permeability homogenization problems for the cells. Additionally, during the optimization process, a continuous approach was assumed and as such the density field of  $\rho$  used values between 0 and 1, with each element of the cell having its own density value. With this, their mechanical and permeability properties can be defined by a power law, where  $K_0$  and  $E_0$  are the base properties and  $\rho$  is a penalization factor, generally used with a value of 4, as this value was the one which yielded optimized solutions that could be realistically used more often (Dias M., 2013). This is considered the solid isotropic material penalization (SIMP) model (Bendsøe & Sigmund, 2004).

$$K = (1 - \rho)^p K_0$$

$$E = \rho^p E_0 \quad (3-14)$$

During the optimization process, the density field has no physical meaning and is instead used to formulate the problem as a continuous optimization problem. Following the SIMP model, the final geometry ideally only has densities of 0 or 1, as long as no failure to converge is met. Elements filled with material ( $\rho=1$ ) are considered to have no permeability and maximum stiffness, while void elements ( $\rho=0$ ) are considered to have no stiffness and maximum permeability. Because of this, the homogenized properties of the resulting topology are normalized to  $E_0$ , the base material stiffness properties, and  $K_0$ , the “void permeability”. While to obtain the effective stiffness, all that is necessary is to multiply the results by the value of the base material, the same cannot be done for  $K_0$ , as it is not easy to define (Dias et al., 2012). Thus, the final values of the permeability property are calculated by homogenizing the Stokes equation. This approach involves a single calculation performed after the optimization process, and it allows for permeability properties to be calculated taking into account the real dimensions of the unit cell. Following Dias et al. (2014), the homogenized Stokes equation can be obtained through solving the microstructure Stokes flow due to unit average pressure gradients:



$$\int_{Y_f} \frac{\partial K_i^j}{\partial y_p} \frac{\partial \varphi_i}{\partial y_p} dY_f = \int_{Y_f} \varphi_j dY_f \quad (3-15)$$

This then leads to the homogenized permeability coefficients being given by:

$$K_{ij}^H = \frac{1}{|Y|} \int_{Y_f} K_i^j dY_f \quad (3-16)$$

As such, FPerm is used as a relative, abstract value for computational comparisons.

The gradients for the effective properties (equations 3-12 and 3-13) are thus:

$$\left\langle \frac{\partial K_{ij}^H}{\partial \rho}, \delta \rho \right\rangle = \frac{1}{|Y|} \int_Y p(1-\rho)^{p-1} K_{sm}^0 \left[ \delta_{is} - \frac{\partial \chi^i}{\partial y_s} \right] \left[ \delta_{jm} - \frac{\partial \chi^j}{\partial y_m} \right] \delta \rho dY \quad (3-17)$$

$$\left\langle \frac{\partial E_{ijk}^H}{\partial \rho}, \delta \rho \right\rangle = \frac{1}{|Y|} \int_Y p \rho^{p-1} E_{pqrs}^0 \left[ \delta_{pi} \delta_{qj} - \frac{\partial \bar{\chi}_p^{ij}}{\partial y_q} \right] \left[ \delta_{kr} \delta_{ms} - \frac{\partial \bar{\chi}_r^{km}}{\partial y_s} \right] \delta \rho dY \quad (3-18)$$

The method of moving asymptotes (MMA) was employed to solve the topology optimization problem itself (Svanberg, 1987), since it was shown to be very well adjusted to solving problems with a high number of design variables, which in this case are the density values for each element of the cell. With the MMA, in each iteration of the optimization tool, a convex and separable sub-problem is generated, allowing dual methods to be used to reduce the computational effort:

$$\begin{aligned} & \text{minimize} \quad \tilde{f}_0(\rho) + a_0 z + \sum_{i=1}^m \left( c_i y_i + \frac{1}{2} d_i y_i^2 \right) \\ & \text{subject to} \quad \tilde{f}_i(\rho) - a_i z - y_i \leq 0, \quad i = 1, \dots, m \\ & \quad \quad \quad \rho \in [\rho^{\min}, \rho^{\max}], \quad y \geq 0, \quad z \geq 0 \end{aligned} \quad (3-19)$$

The functions  $\tilde{f}_i$  depend on the upper and lower asymptotes chosen ( $u_i, l_i$ ), as well as on the gradient of the original functions  $F_i$ , which depend on the sensitivities of the homogenized properties, as given by equations 3-17 and 3-18:

$$\begin{aligned} \tilde{f}_i^{(k)}(\rho) &= \sum_{j=1}^n \left( \frac{p_{ij}^{(k)}}{u_j^{(k)} - \rho_j} + \frac{q_{ij}^{(k)}}{\rho_j - l_j^{(k)}} \right) + r_i^{(k)}, \quad i = 0, 1, \dots, m \\ \begin{cases} p_{ij}^{(k)} = (u_j^{(k)} - \rho_j^{(k)})^2 \left( 1.001 \left( \frac{\partial f_i}{\partial x_j}(\rho^{(k)}) \right)^+ + 1.001 \left( \frac{\partial f_i}{\partial x_j}(\rho^{(k)}) \right)^- + \frac{\rho_i}{\rho_j^{\max} - \rho_j^{\min}} \right) \\ q_{ij}^{(k)} = (\rho_j^{(k)} - l_j^{(k)})^2 \left( 1.001 \left( \frac{\partial f_i}{\partial x_j}(\rho^{(k)}) \right)^+ + 1.001 \left( \frac{\partial f_i}{\partial x_j}(\rho^{(k)}) \right)^- + \frac{\rho_i}{\rho_j^{\max} - \rho_j^{\min}} \right) \end{cases} \end{aligned} \quad (3-20)$$

### 3.2.4 Implementation

This optimization tool was implemented in Fortran 90 following the scheme in **Figure 3.5**, where  $\lambda^*$  is the solution of the dual problem at each iteration, which has an associated sub-problem solution  $\rho^*$ .

After reading the input files defining the problem type to be solved, some of the variables are defined in the sub-routine INITI, such as the minimum and maximum values of density, as well as the initial density field, obtained from the initial solution. Afterwards, the objective function  $F_{obj}$ , constraint functions  $F_i$ , and their gradients are computed in FUNC2, following equations 3-9, 3-10, 3-12, and 3-13.

After this, the iterative process begins and only stops when the maximum number of iterations is reached, or convergence is obtained. This process consists of establishing the lower and upper asymptotes  $u_j$  and  $l_j$ , solving the sub-problem (equation 3-19) by using the sub-routine MMASUB, and using the solution  $p^*$  (updated in the XUPDAT sub-routine) as the next density distribution. Then, the values of  $F_{obj}$  and  $F_i$  are computed again through FUNC2. If convergence is obtained or the maximum number of iterations is reached, these will be the final density distribution and final values of  $F_{obj}$  and  $F_i$ , otherwise, the process iterates once again.

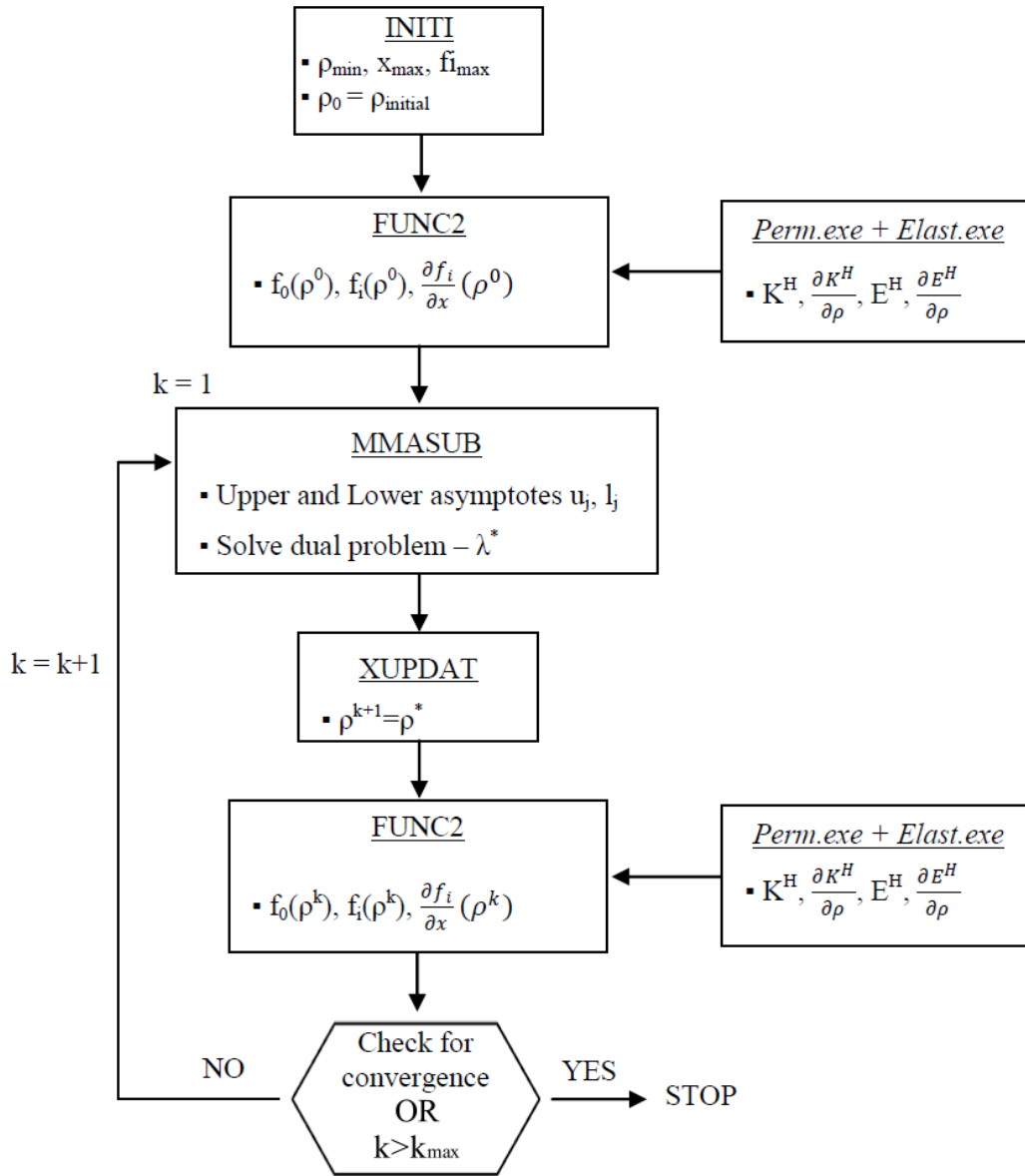


**Figure 3.5:** Representation of the implementation of the optimization tool.

### 3.2.5 Problem types

In this work, the objective functions used were those of FPerm maximization, FElast maximization, and a multi-criteria function where permeability and stiffness properties were weighted. Constraint functions were placed on the volume, FPerm, or FElast. While the amount of material available can be generally restricted by a constraint on VF, this is not necessary in all cases since FPerm and FElast have opposite effects on material requirements. Designs with higher permeability generally have a lower VF, while designs with higher stiffness generally have a higher VF.

Remembering equation 3-10, FElast is affected by  $\varepsilon$ , which means that, if used as an objective or constraint function, the final structure will be optimized for the chosen strain field. This means that the optimized structure can be made tailored to a specific location in the bone as long as the mechanical

conditions of the implantation site are known. **Figure 3.6** shows how topologies maximized for elasticity can vary for different  $\epsilon$ .

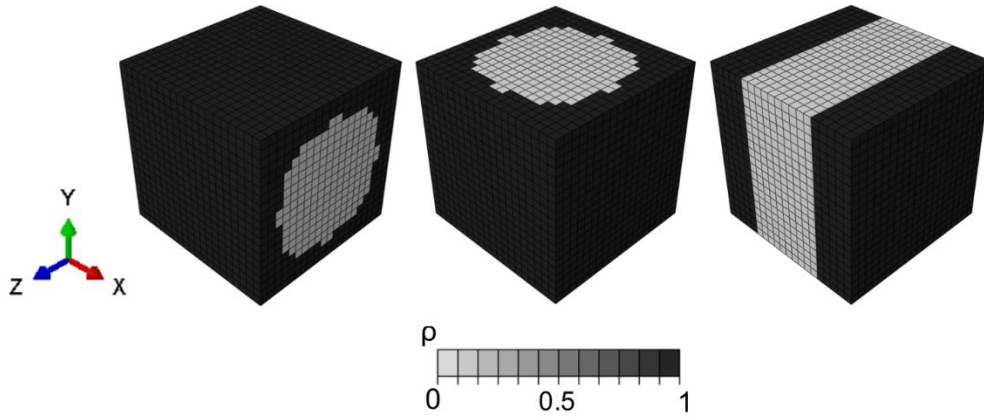


**Figure 3.6:** Topologies optimized for maximized elasticity, with  $VF=50\%$  and initial solution d7 (**Figure 3.4**), under different strain fields. Left: uniaxial in x,  $\epsilon=[1,0,0,0,0,0]$ ; center: uniaxial in y,  $\epsilon=[0,1,0,0,0,0]$ ; right: biaxial in z/y,  $\epsilon=[0,1,1,0,0,0]$ .

### 3.2.5.1 Stiffness optimization problem

To optimize stiffness, the objective function is set as the negative of FElast and constraints are placed on volume and/or FPerm. Because higher FPerm leads to the same behavior as a lower VF, both of these constraints aren't necessarily needed simultaneously. In this problem, the optimization tool finds the highest stiffness properties possible for a constraint on the maximum material used.

$$\text{minimise} \quad -FE_{\text{last}}$$

$$\text{subject to} \quad F_{\text{Perm}} \geq F_{\text{Perm}}^*$$

$$VF \leq VF^*$$

$$0.0001 \leq \rho \leq 0.999 \quad (3-21)$$

### 3.2.5.2 Permeability optimization problem

In permeability optimization, the objective function is set as the inverse of FPerm and constraints are placed on volume and/or FElast. Here, the optimization tool finds the highest permeability properties possible for a constraint on the minimum material that can be used so that mechanical requirements can still be met. Similarly to the previous problem type, both constraint functions here have the same effect, which is that of raising VF.

$$\text{minimise} \quad \frac{1}{F_{\text{Perm}} + 1}$$

$$\text{subject to} \quad FE_{\text{last}} \geq FE_{\text{last}}^*$$

$$VF \geq VF^*$$

$$0.0001 \leq \rho \leq 0.999 \quad (3-22)$$

### 3.2.5.3 Multi-objective problem

The multi-objective problem type uses a multi-criteria objective function where a weight parameter  $\alpha$  can be chosen, and a constraint is placed on volume.

$$\begin{aligned} \text{minimise} \quad & -\alpha F_{\text{Perm}} - (1 - \alpha) F_{\text{Elast}} \\ \text{subject to} \quad & VF = VF^* \\ & 0.0001 \leq \rho \leq 0.999 \end{aligned} \tag{3-23}$$

If  $\alpha$  is set to 0, this becomes a stiffness optimization problem, and if it is set to 1, this becomes a permeability optimization problem.

## 3.3 CFD Permeability

Because the homogenized permeability of the topology is normalized to  $K_0$ , the “void permeability”, which is not easy to define and, per equation 3-16, leads to  $K^H$  having a value between 0 and 1, another method of permeability calculation had to be used so that this property could be better understood and compared to real scenarios. Computational fluid dynamics (CFD) was chosen as the alternate method to calculate scaffold permeability, following procedures used by Pires (2019) and Guerreiro et al. (2020).

The permeability of the scaffolds was calculated using computational fluid dynamics (CFD). The software FLUENT® ANSYS® (Ansys Inc., Canonsburg, Pennsylvania, USA) was used to calculate the  $\nabla P$  of each geometry. Using Equation (3-3),  $\mathbf{K}$  was then obtained, for a  $\mathbf{q}$  of  $3 \times 10^{-6}$  m/s and a  $\mu$  of  $0.001$  Ns/m<sup>2</sup>. To calculate fluid flow in this software, fluid chambers were added before and after the cell to simulate the permeability chamber in the direction of fluid flow, for a length of 3 mm and a model of size 20x40x20, and periodicity conditions were employed. Additionally, because this program works only on the liquid phase, all nodes and elements pertaining solely to solid material had to be removed from the mesh, using a Python script created for this purpose.

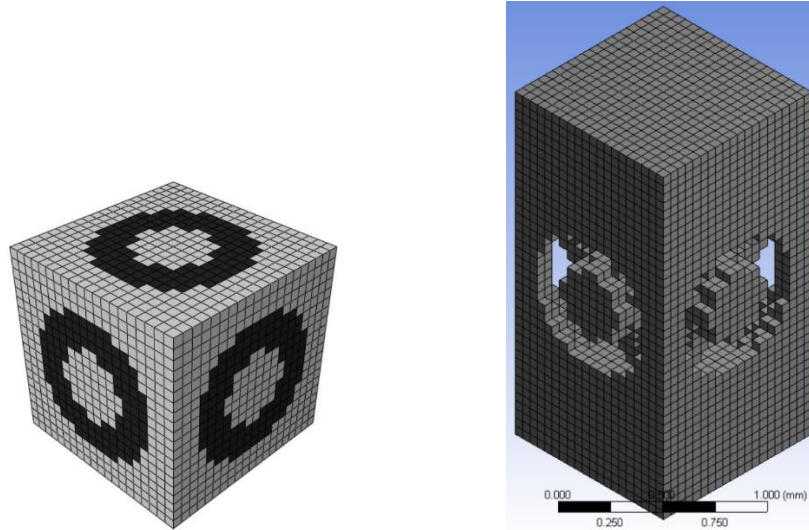


**Figure 3.7:** Left: cell model resulting from the optimization tool; right: the same cell model in FLUENT ® ANSYS ®, after addition of the permeability chamber. It is of note that FLUENT ® ANSYS ® assumes elements not filled with fluid as void, opposite to what is done in the optimization tool.

### 3.4 TPMS geometries

The models for the TPMS topologies created for this work were designed computationally, using the program developed by Dinis et al. (2014). This program receives the desired type of TPMS, the number of cubic elements per side of the cell model, and the + hole size and - hole size parameters. The hole size parameters determine the material quantity to be added on the exterior and interior sides of the surface, which originates a 3D geometry out of the 2D surface. In this work, these two parameters always shared value, to ensure the original surface is in the center of the geometry (Pires, 2019). When it finishes, this program returns the calculated porosity of the scaffold as well as the necessary files for its visualization and printing on a 3D printer.

The Python code of this program was altered so it returned an additional text file that could be read by the optimization tool described in section 3.2, in the same format of the density files it reads, that is, describing the model size and the densities of every element. Additionally, the porosity calculation was altered so it matched equation 3-8.

To maintain coherence with the optimized structures, the TPMS topologies created with this program were all cubic cells of 20 cubic elements per side (**Figure 3.8**).

For this work, nine TPMS topologies were used for comparisons: SP, SD, and SG, with porosities of approximately 60%, 70% and 80%, following previous work (Pires, 2019) (Dias, 2013) (Guerreiro et al., 2020). Reaching these values was not always possible, thus a  $\pm 0.5\%$  margin of deviance was allowed. The properties of these TPMS geometries, which will in the rest of this work be referred to by their geometry and porosity (an SD scaffold with 60% porosity will be called SD60), can be seen on **Table 3.1**.

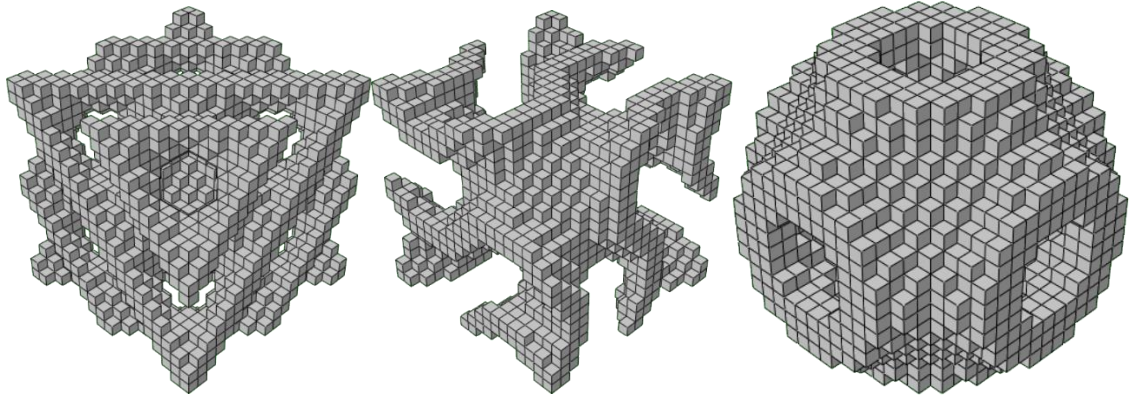


**Figure 3.8:** TPMS with 70% porosity and cell model size of 20x20x20. Left: SD; middle: SG; right: SP.

**Table 3.1:** TPMS geometries used for comparison and their attributes.

TPMS	CFD (mm <sup>2</sup> )	FPerm	Exx	FElast $\epsilon=[1,1,1,0,0,0]$	FElast $\epsilon=[0,0,0,1,1,1]$
SD80	$5.513 \times 10^{-4}$	0.650	$7.542 \times 10^{-2}$	$2.106 \times 10^{-1}$	$2.113 \times 10^{-2}$
SD70	$3.169 \times 10^{-4}$	0.430	$1.253 \times 10^{-1}$	$3.666 \times 10^{-1}$	$4.296 \times 10^{-2}$
SD60	$2.059 \times 10^{-4}$	0.322	$1.904 \times 10^{-1}$	$5.650 \times 10^{-1}$	$7.740 \times 10^{-2}$
SG80	$8.827 \times 10^{-4}$	0.586	$5.090 \times 10^{-2}$	$1.789 \times 10^{-1}$	$3.110 \times 10^{-2}$
SG70	$5.054 \times 10^{-4}$	0.407	$9.156 \times 10^{-2}$	$3.171 \times 10^{-1}$	$5.780 \times 10^{-2}$
SG60	$3.342 \times 10^{-4}$	0.328	$1.513 \times 10^{-1}$	$4.996 \times 10^{-1}$	$9.631 \times 10^{-2}$
SP80	$6.528 \times 10^{-4}$	0.527	$4.227 \times 10^{-2}$	$2.733 \times 10^{-1}$	$4.685 \times 10^{-2}$
SP70	$4.571 \times 10^{-4}$	0.371	$8.567 \times 10^{-2}$	$4.397 \times 10^{-1}$	$8.075 \times 10^{-2}$
SP60	$2.068 \times 10^{-4}$	0.263	$1.550 \times 10^{-1}$	$6.480 \times 10^{-1}$	$1.253 \times 10^{-1}$

## 4 Results and Discussion

The selected TPMS geometries of section 3.4 are here with a series of geometries created with the optimization tool described in section 3.2. Firstly, a varied series of geometries were created using the multi-objective problem type, for a range of parameters, so that the scope of properties of optimized geometries could be better understood. Then, it was explored if the TPMS geometries could be optimized by this tool, and if optimized geometries could be created with the same attributes as the TPMS, from the initial solutions of **Figure 3.4**.

### 4.1 Optimization attribute variability

As described previously in section 2.2, there are multiple variables that change the outcome of an optimized geometry. As such, in order to see the scope of attribute values that these structures can have, the optimization tool was run for the multi-objective problem type, for VF values of 20, 30, and 40, for all initial solutions (see **Figure 3.4**), and for  $\alpha$  values between 0.1 and 0.9, incrementing by 0.1. Not all of the resulting topologies met the VF requirements due to local solutions. Optimized structures were created under these criteria for strain fields  $\epsilon=[1,1,1,0,0,0]$  and  $\epsilon=[0,0,0,1,1,1]$ , representing a triaxial normal strain field and a triaxial shear strain field, respectively. Only solutions with a porosity deviation smaller than 2% from the intended value and lacking “fluid pockets” (structures where a pore of fluid would have no connectivity, which, if printed and subsequently implanted, would eventually degrade and release trapped by-products from the manufacturing process into the body) were considered, and are shown in **Table 4.1** and **Table 4.2**.

It can be initially seen that some parameters were much more likely to lead to a converged solution than others. In **Table 4.1**, it can be seen that the initial solution d7 was more likely to lead to favorable converged solutions, whereas in **Table 4.2** the same can be said for d1 and d4. Additionally, there are more geometries with 60% porosity than of the other porosities. The amount of material at disposal with 60% porosity makes it more likely to obtain a mechanically sound structure, following the requirements of  $F_{obj}$ . In addition, a lot of structures for high porosity values had “fluid pockets”, as the optimization tool sought to reach the required VF by removing material from places where it wouldn’t greatly affect mechanical properties.

For the normal strain field, most of the optimized structures were shaped like SPs (**Figure 4.2**). The higher elastic modulus associated with these structures might have been the cause for this phenomenon (Maskery et al., 2018). For the shear strain field, the majority of the structures were, however, a series of diagonal pillars (**Figure 4.1**). These later ones would realistically not be possible to print, as there is nothing supporting their separate parts. However, because the optimization tool considers them as part of an infinitely periodical structure, the homogenized elasticity coefficients, especially in the directions of the strain field, are computed as generally on the same scale as those of the normal strain field geometries.



**Table 4.1:** Properties of optimized topologies created using the multi-objective problem for the given  $\alpha$  values, initial solutions, VF, and for  $\epsilon=[1,1,1,0,0,0]$ .

Initial solution	$\alpha$	VF (%)	Permeability	FPerm	Exx	FElast $\epsilon=[1,1,1,0,0,0]$	FElast $\epsilon=[0,0,0,1,1,1]$
d7	0.1	80	$2.22 \times 10^{-3}$	0.61	$7.97 \times 10^{-2}$	$1.99 \times 10^{-1}$	$1.87 \times 10^{-2}$
d7	0.1	70	$8.78 \times 10^{-4}$	0.45	$1.17 \times 10^{-1}$	$3.72 \times 10^{-1}$	$5.74 \times 10^{-2}$
d7	0.1	60	$2.59 \times 10^{-4}$	0.23	$1.49 \times 10^{-1}$	$6.46 \times 10^{-1}$	$1.20 \times 10^{-1}$
d7	0.2	80	$2.33 \times 10^{-3}$	0.61	$7.80 \times 10^{-2}$	$1.95 \times 10^{-1}$	$1.78 \times 10^{-2}$
d3	0.2	70	$6.83 \times 10^{-4}$	0.26	$8.78 \times 10^{-2}$	$4.14 \times 10^{-1}$	$6.93 \times 10^{-2}$
d7	0.2	70	$5.04 \times 10^{-4}$	0.41	$8.79 \times 10^{-2}$	$4.14 \times 10^{-1}$	$7.23 \times 10^{-2}$
d7	0.2	60	$2.95 \times 10^{-4}$	0.30	$1.56 \times 10^{-1}$	$6.51 \times 10^{-1}$	$1.21 \times 10^{-1}$
d7	0.3	80	$2.68 \times 10^{-3}$	0.63	$8.52 \times 10^{-2}$	$1.92 \times 10^{-1}$	$1.48 \times 10^{-2}$
d1	0.3	70	$7.35 \times 10^{-4}$	0.45	$1.06 \times 10^{-1}$	$3.70 \times 10^{-1}$	$5.84 \times 10^{-2}$
d7	0.3	70	$5.64 \times 10^{-4}$	0.33	$8.52 \times 10^{-2}$	$4.02 \times 10^{-1}$	$6.99 \times 10^{-2}$
d1	0.3	60	$2.98 \times 10^{-4}$	0.24	$1.51 \times 10^{-1}$	$6.39 \times 10^{-1}$	$1.18 \times 10^{-1}$
d3	0.3	60	$3.31 \times 10^{-4}$	0.24	$1.47 \times 10^{-1}$	$6.32 \times 10^{-1}$	$1.17 \times 10^{-1}$
d7	0.3	60	$2.96 \times 10^{-4}$	0.24	$1.47 \times 10^{-1}$	$6.32 \times 10^{-1}$	$1.18 \times 10^{-1}$
d7	0.4	80	$3.21 \times 10^{-3}$	0.64	$8.59 \times 10^{-2}$	$1.88 \times 10^{-1}$	$1.35 \times 10^{-2}$
d1	0.4	70	$7.21 \times 10^{-4}$	0.34	$8.81 \times 10^{-2}$	$4.16 \times 10^{-1}$	$7.08 \times 10^{-2}$
d7	0.4	70	$5.53 \times 10^{-4}$	0.34	$8.81 \times 10^{-2}$	$4.16 \times 10^{-1}$	$7.25 \times 10^{-2}$
d4	0.4	60	$5.15 \times 10^{-4}$	0.37	$1.49 \times 10^{-1}$	$5.20 \times 10^{-1}$	$1.01 \times 10^{-1}$
d7	0.4	60	$3.30 \times 10^{-4}$	0.25	$1.48 \times 10^{-1}$	$6.26 \times 10^{-1}$	$1.16 \times 10^{-1}$
d1	0.5	70	$7.74 \times 10^{-4}$	0.45	$1.07 \times 10^{-1}$	$3.09 \times 10^{-1}$	$3.57 \times 10^{-2}$
d7	0.5	70	$5.53 \times 10^{-4}$	0.34	$8.81 \times 10^{-2}$	$4.16 \times 10^{-1}$	$7.25 \times 10^{-2}$
d7	0.5	60	$3.42 \times 10^{-4}$	0.34	$1.48 \times 10^{-1}$	$6.23 \times 10^{-1}$	$1.14 \times 10^{-1}$
d7	0.6	80	$2.52 \times 10^{-3}$	0.65	$9.60 \times 10^{-2}$	$1.75 \times 10^{-1}$	$1.03 \times 10^{-2}$
d4	0.6	70	$1.43 \times 10^{-3}$	0.48	$1.14 \times 10^{-1}$	$3.04 \times 10^{-1}$	$5.06 \times 10^{-2}$
d7	0.6	70	$1.22 \times 10^{-3}$	0.49	$1.33 \times 10^{-1}$	$3.37 \times 10^{-1}$	$4.15 \times 10^{-2}$
d6	0.6	60	$3.18 \times 10^{-4}$	0.32	$1.54 \times 10^{-1}$	$6.10 \times 10^{-1}$	$1.11 \times 10^{-1}$
d7	0.6	60	$3.76 \times 10^{-4}$	0.32	$1.49 \times 10^{-1}$	$6.22 \times 10^{-1}$	$1.14 \times 10^{-1}$
d6	0.7	60	$8.37 \times 10^{-4}$	0.37	$2.12 \times 10^{-1}$	$4.96 \times 10^{-1}$	$7.19 \times 10^{-2}$

Figures 4.3 to 4.6 demonstrate that, for most cases, optimized topologies can achieve the same parameters as TPMS, or higher values. For 80% and 70% porosity, the optimized structures obtained all have higher permeability than the TPMS. SG60's permeability falls within the range of values from the optimized geometries, but these still achieve higher permeability values. The Young's modulus Exx of optimized topologies created for a deformation field  $\epsilon=[0,0,0,1,1,1]$  is, as expected, much lower than

that of the other topologies. For  $\varepsilon=[1,1,1,0,0,0]$ , the optimized structures once again show values higher or equal to those of TPMS.

**Table 4.2:** Properties of optimized topologies created using the multi-objective problem for the given  $\alpha$  values, initial solutions, VF, and for  $\varepsilon=[0,0,0,1,1,1]$ .

Initial solution	$\alpha$	VF (%)	Permeability (CFD, mm <sup>2</sup> )	FPerm	Exx	FElast $\varepsilon=[1,1,1,0,0,0]$	FElast $\varepsilon=[0,0,0,1,1,1]$
d1	0.2	80	$3.72 \times 10^{-3}$	0.70	$8.05 \times 10^{-3}$	$1.33 \times 10^{-1}$	$8.46 \times 10^{-2}$
d3	0.2	80	$3.71 \times 10^{-3}$	0.70	$8.05 \times 10^{-3}$	$1.33 \times 10^{-1}$	$8.49 \times 10^{-2}$
d7	0.2	80	$2.02 \times 10^{-3}$	0.62	$1.92 \times 10^{-7}$	$6.31 \times 10^{-7}$	$1.18 \times 10^{-7}$
d1	0.2	70	$2.80 \times 10^{-3}$	0.59	$1.83 \times 10^{-2}$	$2.06 \times 10^{-1}$	$1.19 \times 10^{-1}$
d4	0.2	70	$1.21 \times 10^{-3}$	0.59	$2.26 \times 10^{-7}$	$7.38 \times 10^{-7}$	$1.41 \times 10^{-7}$
d1	0.2	60	$1.08 \times 10^{-3}$	0.48	$3.51 \times 10^{-2}$	$2.95 \times 10^{-1}$	$1.54 \times 10^{-1}$
d4	0.2	60	$6.23 \times 10^{-4}$	0.46	$3.20 \times 10^{-7}$	$9.95 \times 10^{-7}$	$2.01 \times 10^{-7}$
d7	0.2	60	$9.26 \times 10^{-4}$	0.41	$2.94 \times 10^{-2}$	$2.67 \times 10^{-1}$	$1.43 \times 10^{-1}$
d4	0.4	60	$6.27 \times 10^{-4}$	0.46	$3.19 \times 10^{-7}$	$9.93 \times 10^{-7}$	$2.01 \times 10^{-7}$
d7	0.5	80	$2.28 \times 10^{-3}$	0.54	$4.91 \times 10^{-3}$	$1.17 \times 10^{-1}$	$6.16 \times 10^{-3}$
d4	0.5	60	$6.15 \times 10^{-4}$	0.46	$3.51 \times 10^{-2}$	$9.99 \times 10^{-7}$	$2.03 \times 10^{-7}$
d6	0.5	60	$1.02 \times 10^{-3}$	0.42	$3.12 \times 10^{-2}$	$2.76 \times 10^{-1}$	$1.48 \times 10^{-1}$

The same generalizations cannot be made for FElast values. In **Figure 4.5**, it can be seen that once again, the optimized topologies created for  $\varepsilon=[0,0,0,1,1,1]$  underperform. The other optimized topologies have value ranges that encompass the TPMS's totally or partially, with SP70 and SP80 having a higher value, as well as the SD80. In **Figure 4.6**, optimized geometries made for  $\varepsilon=[0,0,0,1,1,1]$  show great variability of FElast values, including both higher and much lower values than the TPMS. Optimized geometries for  $\varepsilon=[1,1,1,0,0,0]$  show a range of FElast values encompassing most of the TPMS, but not reaching as high as the SP60 and SP70. For 80% porosity, all TPMS achieve higher FElast values than these optimized geometries.

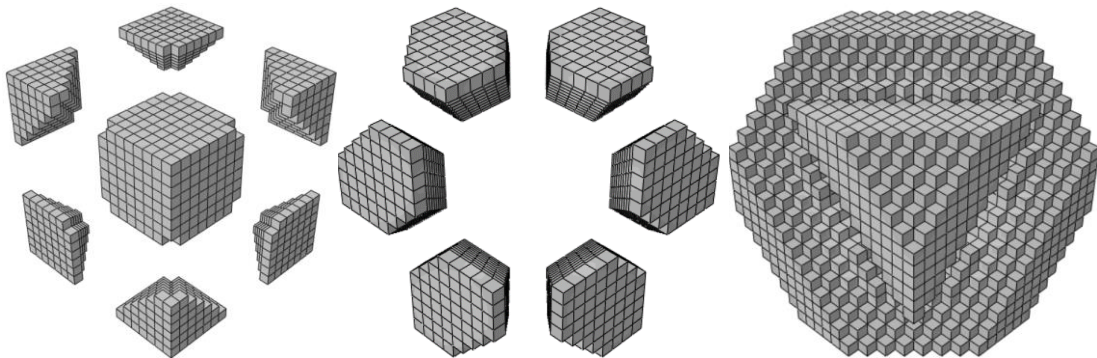


**Figure 4.1:** Some of the geometries described in **Table 4.2**. From left to right, top to bottom: d1,  $\alpha=0.2$ , VF=40; d7,  $\alpha=0.2$ , VF=20; d7,  $\alpha=0.5$ , VF=20.

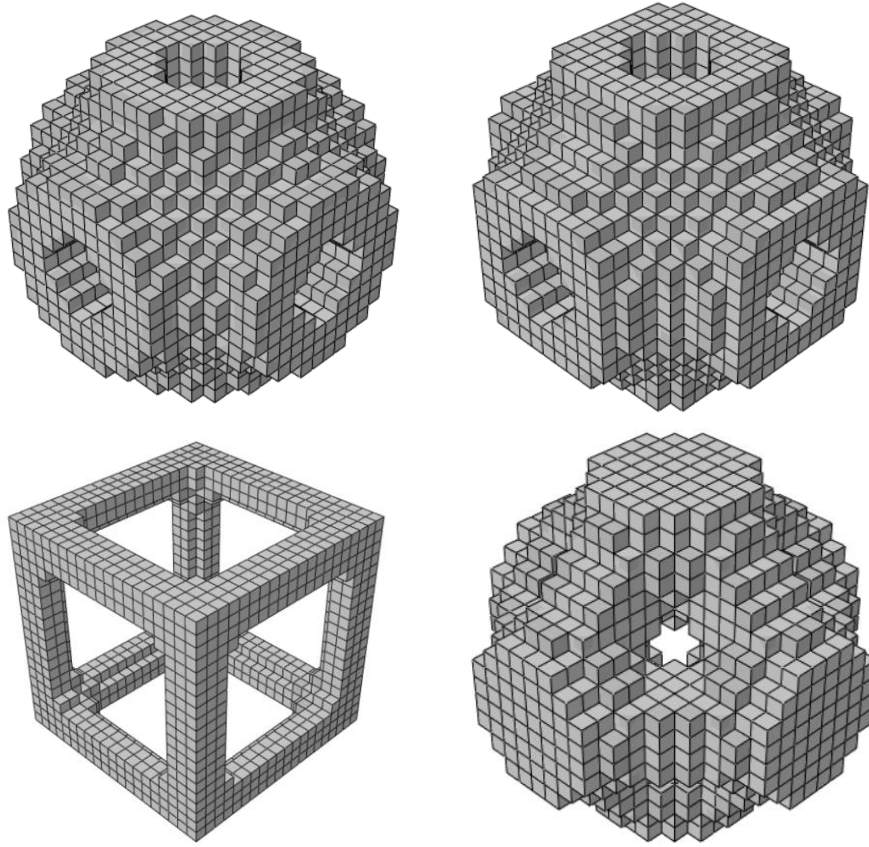


**Figure 4.2:** Some of the geometries described in **Table 4.1**. From left to right, top to bottom: d3,  $\alpha=0.2$ ,  $VF=30$ ; d1,  $\alpha=0.4$ ,  $VF=30$ ; d7,  $\alpha=0.6$ ,  $VF=20$ ; d4,  $\alpha=0.6$ ,  $VF=30$ .

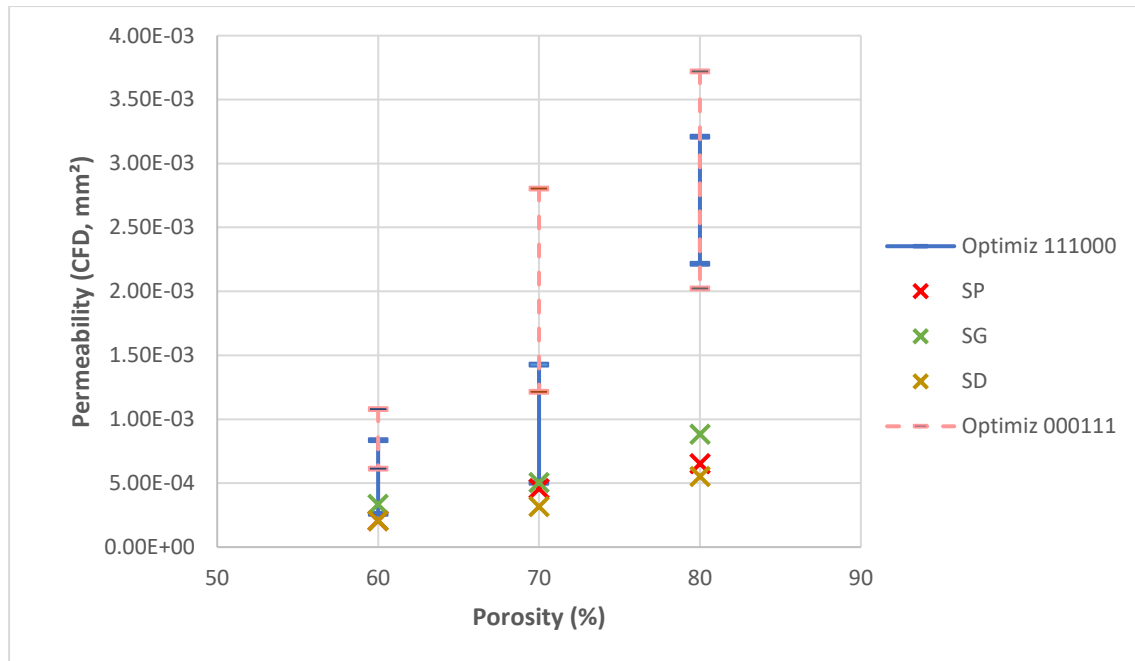


**Figure 4.3:** Range of permeability values for optimized topologies and TPMS.

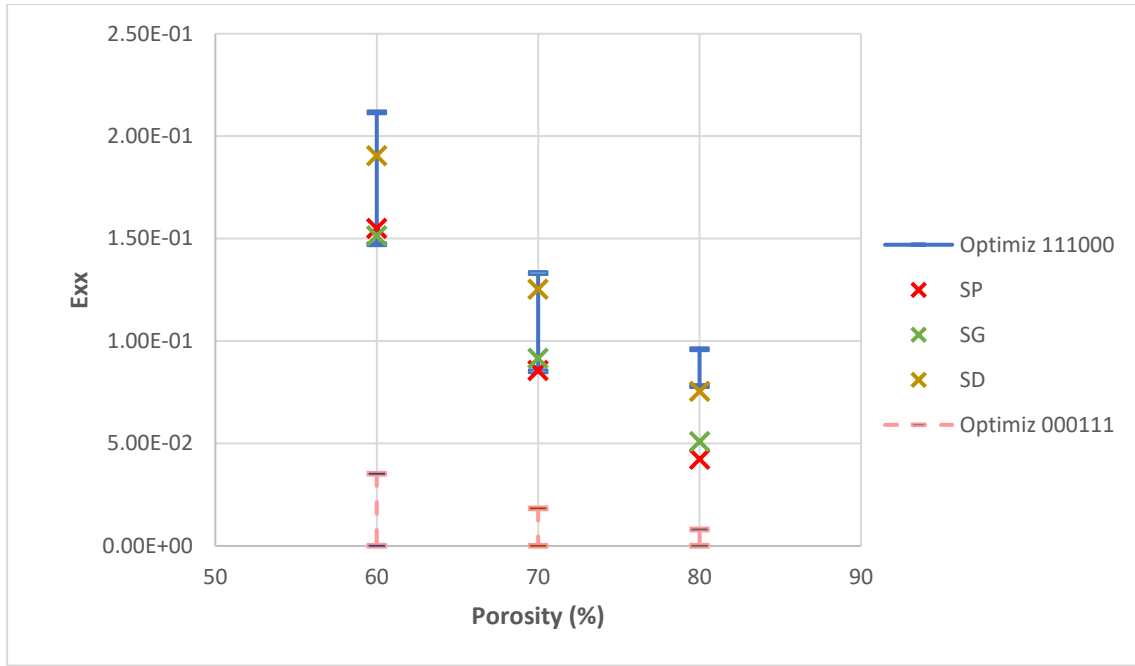


**Figure 4.4:** Range of Young's Modulus values for optimized topologies and TPMS.

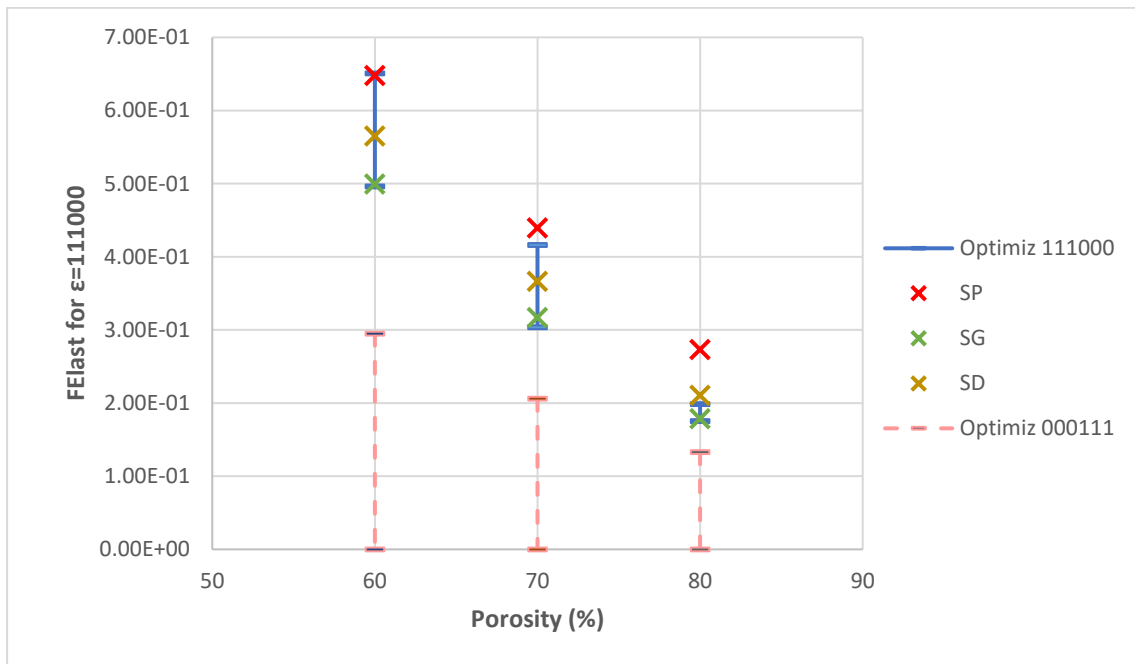


**Figure 4.5:** Range of FElast values for optimized topologies and TPMS, for deformation field  $\varepsilon=[1,1,1,0,0,0]$ .

While there are some specific cases in which optimized geometries cannot replicate the combined attributes of TPMS, the wide choices of initial parameter values allow for wide variety of end results. This means that an optimized geometry can be made to be better tailored to a problem than any TPMS at hand.

**Figure 4.7** helps to emphasize this, showing that for similar rigidity properties, optimized geometries can cover a much wider range of permeability values than TPMS.

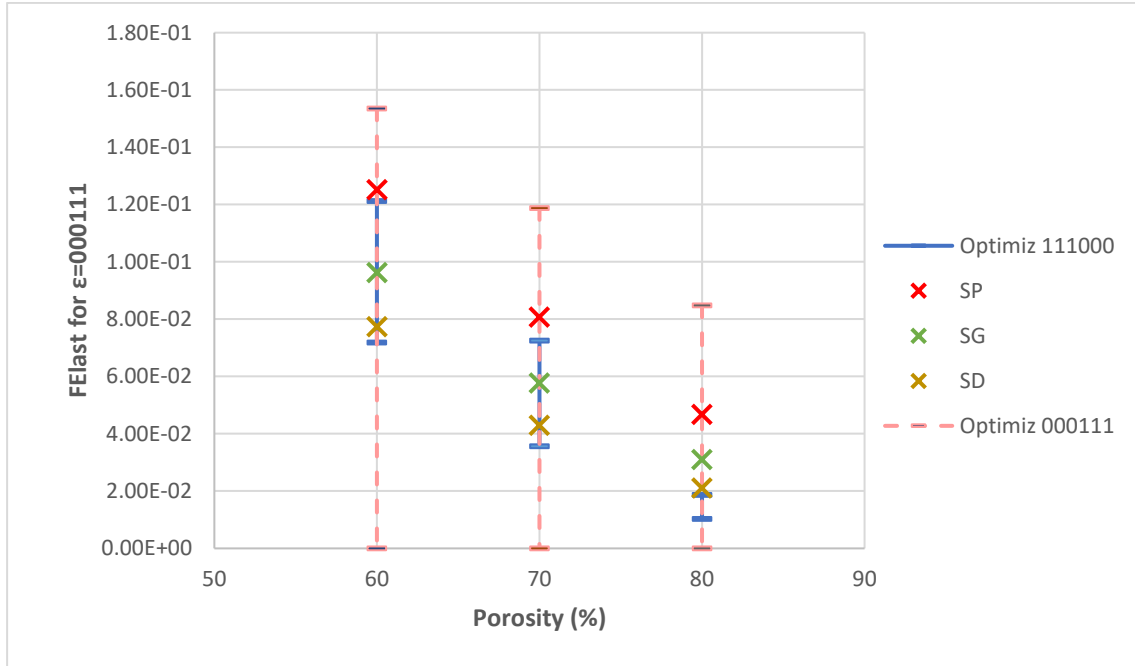


**Figure 4.6:** Range of  $FE_{last}$  values for optimized topologies and TPMS, for deformation field  $\varepsilon=[0,0,0,1,1,1]$ .

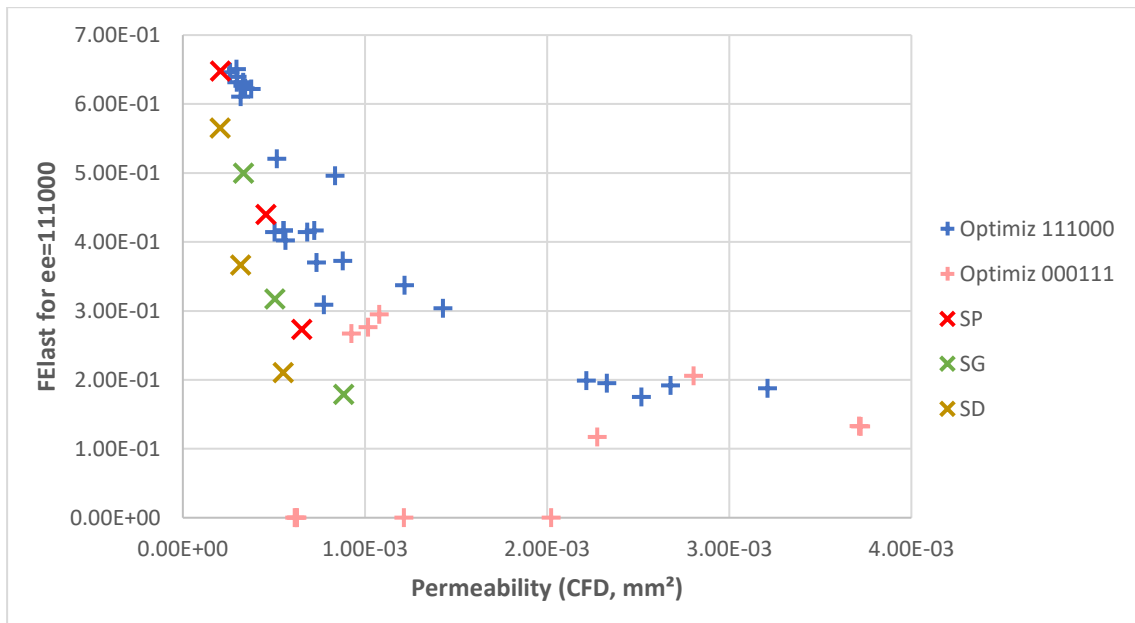


**Figure 4.7:**  $FE_{last}$  and permeability values for the TPMS and all optimized geometries used in this section, for  $\varepsilon=[1,1,1,0,0,0]$ .

## 4.2 Optimizing TPMS geometries

The previously mentioned set of 9 TPMS was used as initial solutions in the optimization tool, with  $\epsilon=[1,1,1,0,0,0]$ . From each of these TPMSs, four different geometries were created: two from the rigidity optimization problem and another two from the permeability optimization problem. For each of these sets of twos, one of the geometries was created utilizing solely the constraint function on the VF, while the other used the two constraint functions of the given problem type.

The objective of these tests was to see if the given TPMS could have their permeability properties optimized, while maintaining the same porosity and elastic properties, or if they could have their elastic properties optimized, while maintaining the same porosity and permeability properties.

The properties of the resulting geometries were very similar or equal to those of the TPMS. As seen in **Table 4.3**, the variations in values are very small, with every attribute showing a maximum deviation an order of magnitude smaller than the original value (see **Table 3.1**), with the exception of porosity, which has a maximum deviation of 3%.

These optimized geometries only suffered minor alterations, an example of which being showcased in **Figure 4.8**. This explains why the attributes retained very similar values.

**Table 4.3:** Maximum deviations of values between TPMS and the optimized structures which used them as initial solutions.

TPMS	Porosity (%)	Permeability (CFD, mm <sup>2</sup> )	FPerm	Exx	FElast $\epsilon=[1,1,1,0,0,0]$
SD60	0.750	0.000	$2.768 \times 10^{-7}$	$1.868 \times 10^{-3}$	$5.316 \times 10^{-3}$
SD70	0.000	0.000	$7.767 \times 10^{-3}$	0.000	0.000
SD80	0.600	$1.610 \times 10^{-5}$	$1.858 \times 10^{-8}$	$2.316 \times 10^{-3}$	$6.781 \times 10^{-3}$
SG60	0.000	0.000	$3.612 \times 10^{-3}$	0.000	$3.000 \times 10^{-8}$
SG70	0.000	0.000	$1.399 \times 10^{-2}$	0.000	$3.000 \times 10^{-8}$
SG80	0.225	$2.426 \times 10^{-5}$	$1.679 \times 10^{-2}$	$3.690 \times 10^{-5}$	$3.403 \times 10^{-3}$
SP60	0.000	0.000	$6.386 \times 10^{-4}$	0.000	$1.500 \times 10^{-7}$
SP70	0.000	0.000	$4.640 \times 10^{-6}$	0.000	$1.000 \times 10^{-8}$
SP80	3.000	0.000	$4.005 \times 10^{-8}$	$7.767 \times 10^{-3}$	$4.073 \times 10^{-2}$
Maximum deviation	3.000	$2.426 \times 10^{-5}$	$1.679 \times 10^{-2}$	$7.767 \times 10^{-3}$	$4.073 \times 10^{-2}$

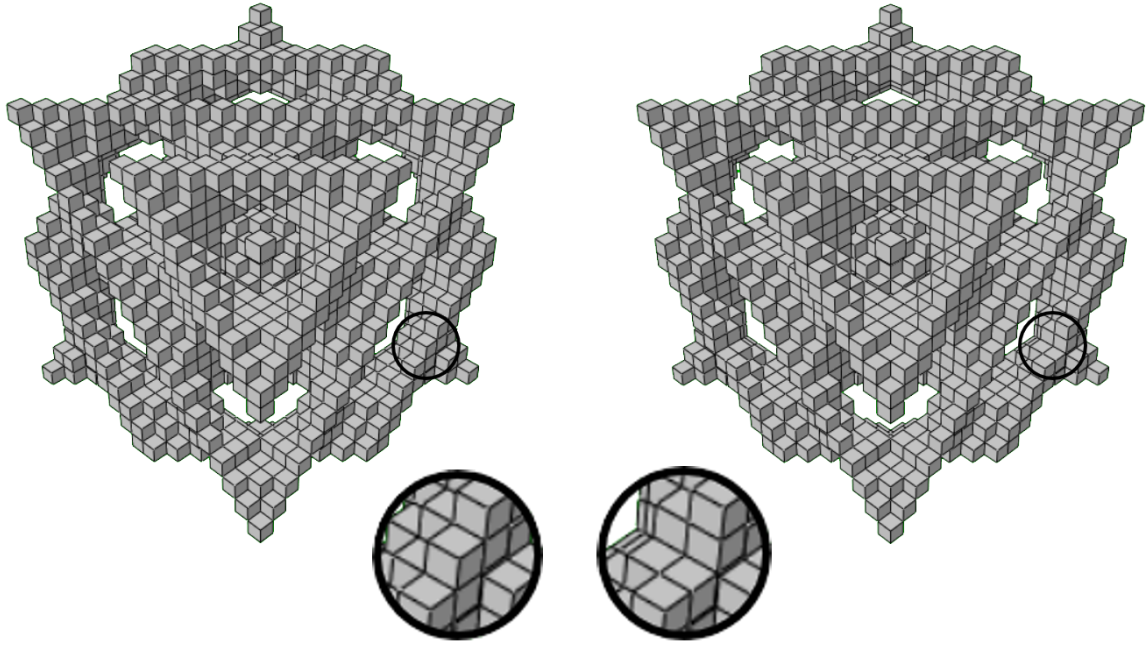


**Figure 4.8:** SD80 (left); resulting geometry of using the rigidity optimization problem using the aforementioned TPMS's porosity and permeability attributes as constraints (right). The black circles indicate one of the design differences.

Because the  $F_{obj}$  to be minimized is not well-behaved (that is, it does not have a single global minimum, but instead has multiple local minimums in addition to the global one), the results given by it are local best solutions. Given that the initial solutions already fulfilled the constraint function requirements, the fact that the objective function could not be further minimized implies that the TPMS structures are already considered a local best.

### 4.3 Replication of TPMS properties

For this section the goal was to create optimized structures with some of the same properties as TPMS. To do this, two sets of nine optimized structures were made, one under the rigidity optimization problem, and the other under the permeability optimization problem. For each set, the properties of the TPMS were used in the constraint functions. All structures used the same initial solution d7 and  $\epsilon=[1,1,1,0,0,0]$ .

Due to the nature of the optimization tool's problem types, it was not always possible to meet both constraint function attribute values, or even optimize the objective function attribute above that of the respective TPMS. The SG80 case under permeability optimization was not considered due to consistently failing to meet constraint function values.

Comparing the values of **Table 3.1** with those of **Table 4.4** and **Table 4.5** (see **Table A1** to view all of the results in one table), a common factor that can be noted is that the structures optimized for permeability will often show higher  $FE_{Elast}$  values than the ones optimized for rigidity. This is because both constraint functions of the later problem type lead to higher porosity and  $F_{Perm}$  values, making it

so that the highest FElast value achievable can become lower. The reverse is observed in the structures optimized for permeability, where their FPerm values are often lower due to the constraint functions pushing for a lower porosity and higher FElast values.

Taking a particular case, the geometry for SG70 in **Table 4.4** keeps almost the exact porosity required but reaches a higher FPerm and thus higher permeability, with a lower FElast. In another example, that of the geometry for SD60 in **Table 4.5**, it can be seen a case where some porosity was sacrificed but all the other attributes managed to obtain higher values than the respective TPMS.

**Table 4.4:** Attributes of nine geometries created from the same initial solution under the rigidity optimization problem. Constraint functions used the VF and FPerm of the respective TPMS.

TPMS	Porosity (%)	Permeability (CFD, mm <sup>2</sup> )	FPerm	Exx	FElast $\epsilon=[1,1,1,0,0,0]$
SD60	62.40	$1.10 \times 10^{-3}$	0.32	$1.32 \times 10^{-1}$	$5.44 \times 10^{-1}$
SD70	70.20	$1.46 \times 10^{-3}$	0.54	$1.49 \times 10^{-1}$	$2.86 \times 10^{-1}$
SD80	89.60	$4.47 \times 10^{-3}$	0.76	$4.32 \times 10^{-2}$	$7.32 \times 10^{-2}$
SG60	64.80	$1.20 \times 10^{-3}$	0.44	$1.84 \times 10^{-1}$	$3.66 \times 10^{-1}$
SG70	69.90	$1.46 \times 10^{-3}$	0.55	$1.52 \times 10^{-1}$	$2.93 \times 10^{-1}$
SG80	79.80	$2.74 \times 10^{-3}$	0.65	$8.11 \times 10^{-2}$	$1.83 \times 10^{-1}$
SP60	59.60	$3.30 \times 10^{-4}$	0.26	$1.51 \times 10^{-1}$	$6.33 \times 10^{-1}$
SP70	70.40	$6.85 \times 10^{-4}$	0.37	$9.74 \times 10^{-2}$	$3.80 \times 10^{-1}$
SP80	79.80	$2.52 \times 10^{-3}$	0.63	$7.73 \times 10^{-2}$	$1.89 \times 10^{-1}$

While some trends can be seen in these tables, such as the increment of FElast as the porosity decreases for each set of optimized geometries replicating properties of a type of TPMS, vast differences in shape can alter some of these trends. For example, for the topologies seen in **Figure 4.9**, FPerm progresses in increments of 0.22 from the one with lowest porosity to the one with highest. However, this proportional increment is not noticed for permeability, due to how the two attributes are calculated and affected differently by porosity and shape of the structure.

When comparing to multi-objective geometries made for  $\alpha=0.5$  and using the initial solution d7 as well, it can be seen that the attributes are still quite similar (**Table 4.6**).

Overall, it cannot be said that the optimization tool in its current state can easily create a topology with the same porosity and FElast (or FPerm) as a pre-existing structure, but with a higher FPerm (or FElast).



**Table 4.5:** Attributes of 8 geometries created from the same initial solution under the permeability optimization problem. Constraint functions used the VF and FElast of the respective TPMS.

TPMS	Porosity (%)	Permeability (CFD, mm <sup>2</sup> )	FPerm	Exx	FElast $\epsilon=[1,1,1,0,0,0]$
<b>SD60</b>	53.70	$8.34 \times 10^{-4}$	0.35	$2.81 \times 10^{-1}$	$6.27 \times 10^{-1}$
<b>SD70</b>	62.70	$2.54 \times 10^{-4}$	0.44	$1.75 \times 10^{-1}$	$4.18 \times 10^{-1}$
<b>SD80</b>	73.30	$1.41 \times 10^{-3}$	0.56	$1.31 \times 10^{-1}$	$2.53 \times 10^{-1}$
<b>SG60</b>	54.30	$8.76 \times 10^{-4}$	0.36	$2.74 \times 10^{-1}$	$6.04 \times 10^{-1}$
<b>SG70</b>	64.00	$1.13 \times 10^{-3}$	0.43	$1.99 \times 10^{-1}$	$4.08 \times 10^{-1}$
<b>SP60</b>	52.80	$5.90 \times 10^{-4}$	0.32	$2.92 \times 10^{-1}$	$6.56 \times 10^{-1}$
<b>SP70</b>	68.30	$4.98 \times 10^{-4}$	0.41	$9.39 \times 10^{-2}$	$4.47 \times 10^{-1}$
<b>SP80</b>	71.20	$2.21 \times 10^{-3}$	0.55	$1.44 \times 10^{-1}$	$2.77 \times 10^{-1}$

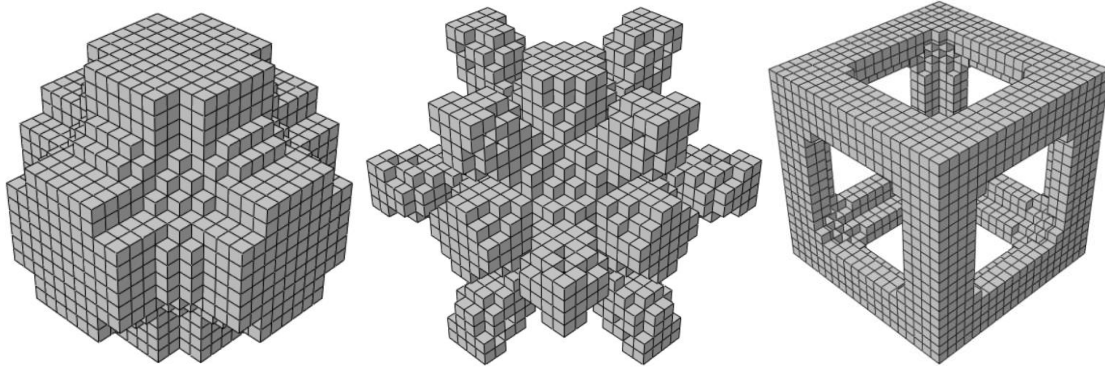


**Figure 4.9:** Some of the optimized structures created under the permeability optimization problem to replicate properties of TPMS SD60 (left); SD70 (center); SD80 (right).

**Table 4.6:** Attributes of 3 optimized geometries created from the same initial solution under the multi-objective optimization problem.

Target Porosity (%)	Porosity (%)	Permeability (CFD, mm <sup>2</sup> )	FPerm	Exx	FElast $\epsilon=[1,1,1,0,0,0]$
<b>60.00</b>	60.20	$3.416 \times 10^{-4}$	0.343	$1.482 \times 10^{-1}$	$6.229 \times 10^{-1}$
<b>70.00</b>	70.20	$5.532 \times 10^{-4}$	0.343	$8.809 \times 10^{-2}$	$4.163 \times 10^{-1}$
<b>80.00</b>	79.60	$2.517 \times 10^{-3}$	0.647	$9.597 \times 10^{-2}$	$1.753 \times 10^{-1}$

## 5 Conclusions and Future Work

The objective of this work was to update a preexisting optimization tool and use it to gain a better understanding of the properties of optimized topologies, in order to determine if they are a viable option, or even a better option than the more widely used TPMS structures. In this section, the results obtained during this work are reviewed, and ideas for future research are discussed.

### 5.1 Conclusions

In order to explore the properties of optimized topologies, a topology optimization tool previously used in Dias (2013) and Dias et al. (2014) had its code updated to Fortran 90, and was changed to allow a series of problem types at the users choice. These problem types are a multi-objective (permeability and elasticity) maximization with a constraint on volume, permeability maximization with constraints on volume and/or elasticity, and elasticity maximization with constraints on volume and/or permeability. This tool was then used to create a variety of optimized geometries by choosing different problem types, initial solutions, and strain fields.

These optimized geometries were then compared with TPMS geometries, which have been more widely researched in regards to their applications in BTE and are generally regarded as a viable choice for scaffold production due to their good mechanical properties and high surface-to-area ratio, although there is still much to learn about their behavior, especially regarding in vivo applications. For this work, a series of 3 different TPMS types were created using the software tool demonstrated in Dinis et al. (2014) for 3 different porosities, totalling nine different geometries.

To explore the range of values that the attributes of optimized topologies can obtain, a series of them were created using the multi-objective problem, for all the initial solutions and porosities used. When comparing attribute values, it could be seen that optimized geometries achieved much wider range of permeability and elasticity values than the TPMS. For the same porosities, optimized topologies could be made to obtain both permeabilities and elasticity values. It is of note that for triaxial normal strain fields, the optimized topologies resulted in SP-like geometries, despite none of the initial solutions being similar to that shape.

When using the chosen TPMS geometries as initial solutions for the optimization tool, it was found that the resulting optimized geometry did not improve upon the original, presenting little to no changes. Given that the objective function to be minimized, which is used to define the problem in the optimization tool, has multiple local minimums in addition to the global minimum, the TPMS structures can be one of these local minimums or local solutions.

Creating optimized geometries from the same initial solution d7 using permeability optimization with a constraint on elasticity or elasticity optimization with a constraint on permeability to obtain the same attributes as the TPMS geometries yielded a series of geometries with attributes in the same scale as

the TPMS ones. Not all geometries were optimized, and those who were tended to show changes in porosity in order to obtain the higher permeability or elasticity.

Overall, optimized topologies were shown to have more specificity and versatility, as they can be created for specific load scenarios and permeability or stiffness requirements. Topology optimization tools such as the one used in this work can be used for a variety of materials and be edited to use other problem types, such as mechanobiology-based optimization algorithms or steady-state Navier-Stokes flow optimization (Boccaccio et al., 2018) (Zhou & Li, 2008).

With this versatility in mind, and given that optimized topologies were shown in this work to also be able to obtain permeability and mechanical properties on par with TPMS geometries, it can be concluded that optimization has a lot of potential not only for scaffold design in BTE but in other areas of tissue engineering as well.

## **5.2 Future Work**

The results obtained throughout this work showcase the importance of studying the capabilities of topology optimization tools and their possible application in BTE. This has given rise to further work regarding not only the optimization tool itself but also the use of optimized topologies.

One of the major drawbacks of the optimization tool used was the limitations in problem construction. In addition to maximizing permeability, elasticity, or a mix of both, other parameters relevant for scaffold construction should be explored, such as surface area, or wall shear stress, which relate to the bioactivity and degradability of the scaffold. For example, it might prove useful to maximize a geometry's mechanical properties to ensure it supports the loads at the implantation site, while placing a constraint on wall shear stress, in order to prevent too-slow degradation.

In addition, the optimization tool did not take into account whether the optimized structure could be printed and safely implanted. For a triaxial shear strain field, the vast majority of the optimal geometries were composed of separate pieces of material. These geometries could only realistically hold shape if printed with solid walls, which would severely affect the scaffold's permeability. In a triaxial normal strain field, this was a much more uncommon phenomenon (only present when elasticity was not taken into consideration). However, structures with "fluid pockets", that is, structures with isolated pores with no connectivity, would be occasionally produced, more commonly for the highest porosity used: 80%. While these do not produce a great impact on the mechanical properties and aid in meeting VF requirements, these pores could end up filled with toxic materials during the printing process. Following scaffold degradation, these materials are released, making it unsuitable for use in tissue engineering. In the future, it would be ideal for the optimization tool to identify and avoid outputting geometries having such incompatibilities with the manufacturing process.

Further research on the applicability of optimized topologies for BTE is also needed. Ultimately, it is through ex-vivo and in-vivo testing that we might better understand if optimized topologies do meet the requirements of scaffolds in BTE.

## Bibliography

- Abueidda, D., Elhebeary, M., Shiang, C. S. (Andrew), Pang, S., Abu Al-Rub, R. K., & Jasiuk, I. M. (2019). *Mechanical properties of 3D printed polymeric Gyroid cellular structures: Experimental and finite element study*. Materials and Design, 165, 107597.
- Ali, D., Ozalp, M., Blanquer, S. B. G., & Onel, S. (2020). *Permeability and fluid flow-induced wall shear stress in bone scaffolds with TPMS and lattice architectures: A CFD analysis*. European Journal of Mechanics, B/Fluids, 79, pp. 376–385.
- Bahraminasab, M. (2020). *Challenges on optimization of 3D-printed bone scaffolds*. BioMedical Engineering Online, 19(1), pp. 1–33.
- Bendsøe, M., & Kikuchi, N. (1988). *Generating optimal topologies in structural design using a homogenization method*. Computer Methods in Applied Mechanics and Engineering, 71(2), pp. 197–224.
- Bendsøe, M., & Sigmund, O. (2004). *Topology Optimization - Theory, Methods, and Applications*. Springer Berlin Heidelberg.
- Boccaccio, A., Fiorentino, M., Uva, A. E., Laghetti, L. N., & Monno, G. (2018). *Rhombicuboctahedron unit cell based scaffolds for bone regeneration: geometry optimization with a mechanobiology – driven algorithm*. Materials Science and Engineering C, 83, pp. 51–66.
- Boyce, T., Edwards, J., & Scarborough, N. (1999). *Allograft bone: The influence of processing on safety and performance*. Orthopedic Clinics of North America, 30(4), pp. 571–581.
- Castilho, M., Rodrigues, J., Vorndran, E., Gbureck, U., Quental, C., Folgado, J., & Fernandes, P. R. (2017). *Computational design and fabrication of a novel bioresorbable cage for tibial tuberosity advancement application*. Journal of the Mechanical Behavior of Biomedical Materials, 65, pp. 344–355.
- Castro, , A., Santos, J., Pires, T., & Fernandes, P. R. (2020). *Micromechanical Behavior of TPMS Scaffolds for Bone Tissue Engineering*. Macromolecular Materials and Engineering, 2000487, pp. 1–10.
- Castro, A., Ruben, R. B., Gonçalves, S. B., Pinheiro, J., Guedes, J. M., & Fernandes, P. R. (2019). *Numerical and experimental evaluation of TPMS Gyroid scaffolds for bone tissue engineering*. Computer Methods in Biomechanics and Biomedical Engineering, 22(6), pp. 567–573.
- Chocholata, P., Kulda, V., & Babuska, V. (2019). *Fabrication of scaffolds for bone-tissue regeneration*. Materials, 12(4), 568.
- Coelho, P. (2009). *Modelos hierárquicos para a análise e síntese de estruturas e materiais com aplicações à remodelação óssea*. [Doctoral dissertation, Faculdade de Ciências e Tecnologia - Universidade Nova de Lisboa].

- Dabrowski, B., Swieszkowski, W., Godlinski, D., & Kurzydowski, K. J. (2010). *Highly porous titanium scaffolds for orthopaedic applications*. Journal of biomedical materials research. Part B, Applied biomaterials, 95(1), pp. 53–61.
- Dias, M. (2013). *Scaffold Design for Bone Tissue Engineering*. [Doctoral dissertation, Instituto Superior Técnico].
- Dias, M., Fernandes, P. R., Guedes, J. M., & Hollister, S. J. (2012). *Permeability analysis of scaffolds for bone tissue engineering*. Journal of Biomechanics, 45(6), pp. 938–944.
- Dias, M., Guedes, J. M., Flanagan, C. L., Hollister, S. J., & Fernandes, P. R. (2014). *Optimization of scaffold design for bone tissue engineering: A computational and experimental study*. Medical Engineering and Physics, 36(4), pp. 448–457.
- Dinis, J., Morais, T. F., Amorim, P. H. J., Ruben, R. B., Almeida, H. A., Inforçati, P. N., . . . Silva, J. V. L. (2014). *Open Source Software for the Automatic Design of Scaffold Structures for Tissue Engineering Applications*. Procedia Technology, 16(December), pp. 1542–1547.
- Dong, Z., & Zhao, X. (2021). *Application of TPMS Structure in Bone Regeneration*. Dong, Z., & Zhao, X. (2021). . Engineered Regeneration, 2(August), pp. 154–162.
- Dumitrescu, C., Neacsu, I. A., Surdu, V. A., Nicoara, A. I., Iordache, F., Trusca, R., . . . Andronesu, E. (2021). *Nano-hydroxyapatite vs. Xenografts: Synthesis, characterization, and in vitro behavior*. Nanomaterials, 11(9), pp. 1–19.
- Egan, P. (2019). *Integrated design approaches for 3D printed tissue scaffolds: Review and outlook*. Materials, 12(15), 2355.
- Egan, P., Gonella, V. C., Engelsperger, M., Ferguson, S. J., & Shea, K. (2017). *Computationally designed lattices with tuned properties for tissue engineering using 3D printing*. PLoS ONE, 12(8), pp. 1–20.
- Ghattas, O., & Orozco, C. (1997). *A parallel reduced Hessian SQP method for shape optimization*. Multidisciplinary Design Optimization: State of the Art, 15213, pp. 1–20.
- Guedes, J., & Kikuchi, N. (1990). *Preprocessing and postprocessing for materials based on the homogenization method with adaptive finite element methods*. Computer Methods in Applied Mechanics and Engineering, 83(2), pp. 143–198.
- Guerreiro, R., Pires, T., Guedes, J. M., Fernandes, P., & Castro, A. (2020). *On the Tortuosity of TPMS Scaffolds for Tissue Engineering*. Symmetry, 12(4), pp. 596.
- Habib, F., Nikzad, M., Masood, S. H., & Saifullah, A. B. M. (2016). *Design and development of scaffolds for tissue engineering using three-dimensional printing for bio-based applications*. 3D Printing and Additive Manufacturing, 3(2), pp. 119–127.

- Jiang, W., Cipriano, A. F., Tian, Q., Zhang, C., Lopez, M., Sallee, A., . . . Liu, H. (2018). *In vitro evaluation of MgSr and MgCaSr alloys via direct culture with bone marrow derived mesenchymal stem cells*. *Acta Biomaterialia*, 72, pp. 407–423.
- Kladovasilakis, N., Tsongas, K., & Tzetzis, D. (2021). *Mechanical and fea-assisted characterization of fused filament fabricated triply periodic minimal surface structures*. *Journal of Composites Science*, 5(2):58.
- Langer, R., & Vacanti, J. (1993). *Tissue engineering*. *Science*, 260(5110), pp. 920–926.
- LeGeros, R. (2002). *Properties of osteoconductive biomaterials: Calcium phosphates*. *Clinical Orthopaedics and Related Research*, 395, pp. 81–98.
- Lin, C.-Y., Hsiao, C.-C., Chen, P.-Q., & Hollister, S. J. (2004). *Interbody Fusion Cage Design Using Integrated Global Layout and Local Microstructure Topology Optimization*. *Spine*, 29(16), pp. 1747–1754.
- Lin, C.-Y., Wirtz, T., LaMarca, F., & Hollister, S. (2007). *Structural and mechanical evaluations of a topology optimized titanium interbody fusion cage fabricated by selective laser melting process*. *Journal of Biomedical Materials Research. Part A*, 83(2), 272–279.
- Liu, X., & Ma, P. (2004). *Polymeric Scaffolds for Bone Tissue Engineering*. *Annals of Biomedical Engineering*, 32(3), pp. 477–486.
- Lv, J., Jia, Z., Li, J., Wang, Y., Yang, J., Xiu, P., . . . Liu, Z. (2015). *Electron Beam Melting Fabrication of Porous Ti6Al4V Scaffolds: Cytocompatibility and Osteogenesis*. *Advanced Engineering Materials*, 17(9), pp. 1391–1398.
- Maskery, I., Sturm, L., Aremu, A. O., Panesar, A., Williams, C. B., Tuck, C. J., . . . Hague, R. J. M. (2018). *Insights into the mechanical properties of several triply periodic minimal surface lattice structures made by polymer additive manufacturing*. *Polymer*, 152, pp. 62–71.
- Neuman, S. (1977). *Theoretical derivation of Darcy's law*. *Acta Mechanica* 25, pp. 153–170.
- O'Brien, F., Harley, B. A., Yannas, I. V., & Gibson, L. J. (2005). *The effect of pore size on cell adhesion in collagen-GAG scaffolds*. *Biomaterials*, 26(4), pp. 433–441.
- Olhoff, N., & Taylor, J. (1983). *On structural optimization*. *Journal of Applied Mechanics, Transactions ASME*, 50(4), pp. 1139–1151.
- Pires, T. (2019). *Computational fluid dynamics simulation of TPMS scaffolds for bone tissue engineering*. [Masters' thesis, Instituto Superior Técnico].
- Porter, J., Ruckh, T. T., & Popat, K. C. (2009). *Bone tissue engineering: A review in bone biomimetics and drug delivery strategies*. *Biotechnology Progress*, 25(6), pp. 1539–1560.

- Rosso, S., Savio, G., Uriati, F., Meneghello, R., & Concheri, G. (2019). *Optimization approaches in design for additive manufacturing*. Proceedings of the International Conference on Engineering Design, ICED, 2019-August(AUGUST), pp. 809–818.
- Ryan, G., Pandit, A., & Apatsidis, D. P. (2006). *Fabrication methods of porous metals for use in orthopaedic applications*. Biomaterials, 27(13), pp. 2651–2670.
- Shi, J., Zhu, L., Li, L., Li, Z., Yang, J., & Wang, X. (2018). *A TPMS-based method for modeling porous scaffolds for bionic bone tissue engineering*. Scientific Reports, 8(1) pp. 7395.
- Sohn, H., & Oh, J. (2019). *Review of bone graft and bone substitutes with an emphasis on fracture surgeries*. Biomaterials Research, 23(1), pp. 4–10.
- Stevens, M. (2008). *Biomaterials for bone tissue engineering*. Materials Today, 11(5), pp 18–25.
- Sturm, S., Zhou, S., Mai, Y. W., & Li, Q. (2010). *On stiffness of scaffolds for bone tissue engineering-a numerical study*. Journal of Biomechanics, 43(9), pp. 1738–1744.
- Svanberg, K. (1987). *The Method of Moving Asymptotes -A New Method for Structural Optimization*. International Journal for Numerical Methods in Engineering, 24, pp. 359–373.
- Torquato, S., & Donev, A. (2004). *Minimal surfaces and multifunctionality*. Proceedings of the Royal Society A: Mathematical, Physical and Engineering Sciences, 460(2047), pp. 1849–1856.
- Tortora, G., & Derrickson, B. (2016). *Principles of Anatomy and Physiology*. 15th ed. John Wiley & Sons, pp. 171-178.
- Turnbull, G., Clarke, J., Picard, F., Riches, P., Jia, L., Han, F., . . . Shu, W. (2018). *3D bioactive composite scaffolds for bone tissue engineering*. Bioactive Materials, 3(3), pp. 278–314.
- Viola, J., Lal, B., & Grad, O. (2003). *The emergence of tissue engineering as a research field*. National Science Foundation, Arlington, VA, pp. 18–24.
- Williams, J., Adewunmi, A., Schek, R. M., Flanagan, C. L., Krebsbach, P. H., Feinberg, S. E., . . . Das, S. (2005). *Bone tissue engineering using polycaprolactone scaffolds fabricated via selective laser sintering*. Biomaterials, 26(23), pp. 4817–4827.
- Yoo, D.-J. (2014). *Advanced Porous Scaffold Design using Multi-Void Triply Periodic Minimal Surface Models with High Surface Area to Volume Ratios*. International Journal of Precision Engineering and Manufacturing, 15, pp. 1657–1666.
- Zadpoor, A. (2015). *Bone tissue regeneration: The role of scaffold geometry*. Biomaterials Science, 3(2), pp. 231–245.
- Zhang, H., Zhou, L., & Zhang, W. (2014). *Control of scaffold degradation in tissue engineering: A review*. Tissue Engineering - Part B: Reviews, 20(5), pp. 492–502.

- Zhao, H., Han, Y., Pan, C., Yang, D., Wang, H., Wang, T., . . . Su, P. (2021). *Design and mechanical properties verification of gradient voronoi scaffold for bone tissue engineering*. *Micromachines*, 12(6), pp. 1–23.
- Zhou, S., & Li, Q. (2008). *A variational level set method for the topology optimization of steady-state Navier-Stokes flow*. *Journal of Computational Physics*, 227(24), pp. 10178–10195.



## Appendix

### Replication of TPMS properties – full table

**Table A1:** Attributes of TPMS and 18 geometries created from the same initial solution under the rigidity and permeability optimization problems. Constraint functions used the attributes of the respective TPMS. RO: rigidity optimization problem; PO: permeability optimization problem.

	TPMS	SD60	SD70	SD80	SG60	SG70	SG80	SP60	SP70	SP80
Porosity (%)	TPMS	60	70	80	60	70	80	60	70	80
	RO	62.40	70.20	89.60	64.80	69.90	79.80	59.60	70.40	79.80
	PO	53.70	62.70	73.30	54.30	64.00	--	52.80	68.30	71.20
Permeability (CFD, mm <sup>2</sup> )	TPMS	2.06×10 <sup>-4</sup>	3.17×10 <sup>-4</sup>	5.51×10 <sup>-4</sup>	3.34×10 <sup>-4</sup>	5.05×10 <sup>-4</sup>	8.83×10 <sup>-4</sup>	2.07×10 <sup>-4</sup>	4.57×10 <sup>-4</sup>	6.53×10 <sup>-4</sup>
	RO	1.10×10 <sup>-3</sup>	1.46×10 <sup>-3</sup>	4.47×10 <sup>-3</sup>	1.20×10 <sup>-3</sup>	1.46×10 <sup>-3</sup>	2.74×10 <sup>-3</sup>	3.30×10 <sup>-4</sup>	6.85×10 <sup>-4</sup>	2.52×10 <sup>-3</sup>
	PO	8.34×10 <sup>-4</sup>	2.54×10 <sup>-4</sup>	1.41×10 <sup>-3</sup>	8.76×10 <sup>-4</sup>	1.13×10 <sup>-3</sup>	--	5.90×10 <sup>-4</sup>	4.98×10 <sup>-4</sup>	2.21×10 <sup>-3</sup>
FPerm	TPMS	0.32	0.43	0.65	0.33	0.41	0.59	0.26	0.37	0.53
	RO	0.32	0.54	0.76	0.44	0.55	0.65	0.26	0.37	0.63
	PO	0.35	0.44	0.56	0.36	0.43	--	0.32	0.41	0.55
Exx	TPMS	1.90×10 <sup>-1</sup>	1.25×10 <sup>-1</sup>	7.54×10 <sup>-2</sup>	1.51×10 <sup>-1</sup>	9.16×10 <sup>-2</sup>	5.09×10 <sup>-2</sup>	1.55×10 <sup>-1</sup>	8.57×10 <sup>-2</sup>	4.23×10 <sup>-2</sup>
	RO	1.32×10 <sup>-1</sup>	1.49×10 <sup>-1</sup>	4.32×10 <sup>-2</sup>	1.84×10 <sup>-1</sup>	1.52×10 <sup>-1</sup>	8.11×10 <sup>-2</sup>	1.51×10 <sup>-1</sup>	9.74×10 <sup>-2</sup>	7.73×10 <sup>-2</sup>
	PO	2.81×10 <sup>-1</sup>	1.75×10 <sup>-1</sup>	1.31×10 <sup>-1</sup>	2.74×10 <sup>-1</sup>	1.99×10 <sup>-1</sup>	--	2.92×10 <sup>-1</sup>	9.39×10 <sup>-2</sup>	1.44×10 <sup>-1</sup>
F elast $\epsilon=[1,1,1,0,0,0]$	TPMS	5.65×10 <sup>-1</sup>	3.67×10 <sup>-1</sup>	2.11×10 <sup>-1</sup>	5.00×10 <sup>-1</sup>	3.17×10 <sup>-1</sup>	1.79×10 <sup>-1</sup>	6.48×10 <sup>-1</sup>	4.40×10 <sup>-1</sup>	2.73×10 <sup>-1</sup>
	RO	5.44×10 <sup>-1</sup>	2.86×10 <sup>-1</sup>	7.32×10 <sup>-2</sup>	3.66×10 <sup>-1</sup>	2.93×10 <sup>-1</sup>	1.83×10 <sup>-1</sup>	6.33×10 <sup>-1</sup>	3.80×10 <sup>-1</sup>	1.89×10 <sup>-1</sup>
	PO	6.27×10 <sup>-1</sup>	4.18×10 <sup>-1</sup>	2.53×10 <sup>-1</sup>	6.04×10 <sup>-1</sup>	4.08×10 <sup>-1</sup>	--	6.56×10 <sup>-1</sup>	4.47×10 <sup>-1</sup>	2.77×10 <sup>-1</sup>